DEPARTAMENT OF
MECHANICAL AND INDUSTRIAL ENGINEERING

Guilherme Lopes Gamito
BSc in Mechanical Engineering Sciences

Maraging Steel Fabricated via Directed Energy Deposition: Process Parameters Development and Study of the Post-Deposition Aging Heat Treatment

INTEGRATED MASTER IN MECHANICAL ENGINEERING
NOVA University Lisbon
September, 2025

DEPARTMENT OF
MECHANICAL AND INDUSTRIAL ENGINEERING

Maraging Steel Fabricated via Directed Energy Deposition: Process Parameters Development and Study of the Post-Deposition Aging Heat Treatment

Guilherme Lopes Gamito

BSc in Mechanical Engineering Sciences

Adviser: Valdemar Rebelo Duarte
Invited Assistant Professor, NOVA University Lisbon

Co-advisers: Carla Maria Moreira Machado
Assistant Professor, NOVA University Lisbon

Examination Committee:

Chair: Catarina Isabel Silva Vidal
Auxiliar Professor, *NOVA* University Lisbon

Rapporteurs: Francisco Werley Cipriano Farias
PhD Specialist in Additive Manufacturing, Federal University of Rio de Janeiro
Tiago Miguel André Rodrigues
PhD Specialist in Additive Manufacturing, Norks Titanium AS

Adviser: Valdemar Rebelo Duarte
Invited Assistant Professor, *NOVA* University Lisbon

INTEGRATED MASTER IN MECHANICAL ENGINEERING

NOVA University Lisbon
September, 2025

Maraging Steel Fabricated via Directed Energy Deposition: Process Parameters Development and Study of the Post-Deposition Aging Heat Treatment

To those who walked this path with me

ACKNOWLEDGMENT

Thus comes the end of this five-year academic journey, crowned with the completion of this thesis. Its creation was made possible thanks to the inspiration and presence of several people who, in unique ways, shaped this journey.

I extend my deep gratitude to my advisor, Professor Valdemar Duarte, for his time, knowledge, and guidance that turned obstacles into opportunities for growth; to Professor Carla Machado for her specialized contributions that enriched this thesis; and to Mr. Campos and Mr. Paulo for their invaluable workshop assistance, which inspired and strengthened my passion for this work.

To my friends and colleagues who have pushed me through this challenge and who have contributed not only to my academic life, but also to my personal life. Special thanks to my "lab wifey" for helping me in the workshop, for the paid coffees that allowed me to finish the project, and for encouraging me to give my best and complete it with excellence.

To my second family, Amendoinha, for being a driving force behind this work and academic journey. Your friendship and support made this journey easier and more unforgettable. Every moment and laugh shared will always be with me.

To my parents, thank you for everything over these five years. No matter how difficult the situations are, you always encouraged me, believed in me, and taught me that education goes beyond books; it lies in perseverance and responsibility. My sister, for being a haven of refuge and putting up with me on the weekends we saw each other.

Without you, this wouldn't have been possible.

This work was developed under the project "Agenda Drivolution - Transição para a fábrica do futuro" (C644913740-00000022) - Aviso 2021-C05i01-01 PRR, funded by IAPMEI - Agência para a Competitividade e Inovação, I. P., within the scope of the Portuguese "Plano de Recuperação e Resiliência (PRR)" / União Europeia - NextGenerationEU.

“To the optimist, the glass is half full. To the pessimist, the glass is half empty.
To the engineer, the glass is twice as big as it needs to be.” - Unknown

ABSTRACT

The additive manufacturing of Maraging Steels using Directed Energy Deposition Arc (DED-Arc) offers significant potential for producing high-strength and tough components making it attractive for aerospace and tooling applications. However, their precipitation hardening nature and high alloy content make them extremely sensitive to thermal cycles, leading to heterogeneous microstructures and anisotropic properties, which limits industrial adoption.

In this work, a Design of Experiments (DoE) method was applied to optimize deposition parameters (voltage, wire feed speed, and travel speed) based on arc stability, checked through voltage signal analysis. After optimization, a conventional aging heat treatment (480 °C for 5 h) was performed to promote precipitation hardening. Mechanical properties were assessed through uniaxial tensile testing, complemented by optical microscopy and fractography.

The optimized process parameters yielded an arc stability of up to 96%, enabling consistent, defect free deposits. As-built samples exhibited anisotropy, with vertical specimens outperforming horizontal ones in strength and ductility. Aging treatment significantly improved mechanical properties and reduced anisotropy, with mean ultimate tensile strength reaching 1650 MPa. Microstructural analysis revealed a martensitic matrix with reverted austenite and precipitation hardening after aging.

These results demonstrate that the combined optimization of deposition parameters and standard aging treatment enables the production of high-performance maraging steel components using the DED-Arc process.

Keywords: DED-Arc, Maraging Steel, Deposition Parameters, Heat treatment, DoE

RESUMO

A fabricação aditiva de aços Maraging com o processo Directed Energy Deposition Arc (DED-Arc) tem grande potencial para a produção de componentes com elevada resistência e tenacidade, sendo uma atrativa para aplicações aeroespaciais e de moldes. No entanto, a sua natureza de endurecimento por precipitação e o elevado teor de liga tornam estes aços extremamente sensíveis a ciclos térmicos, conduzindo à formação de microestruturas heterogéneas e propriedades anisotrópicas, o que limita a sua adoção industrial.

Neste trabalho, aplicou-se a metodologia de Design of Experiments (DoE) para otimizar os parâmetros de deposição (tensão, velocidade de alimentação e de avanço), com base na estabilidade do arco elétrico, avaliada através da análise do sinal de tensão. Após a otimização, realizou-se um tratamento térmico de envelhecimento convencional (480 °C durante 5 h) para promover o endurecimento por precipitação. As propriedades mecânicas foram avaliadas por ensaios de tração uniaxial, complementados por microscopia ótica e fractografia.

Os parâmetros otimizados permitiram atingir estabilidade do arco de até 96%, obtendo depósitos consistentes e isentos de defeitos. As amostras "as-built" apresentaram anisotropia, com provetes verticais exibindo melhores valores de resistência e ductilidade que os horizontais. O envelhecimento melhorou significativamente as propriedades mecânicas e reduziu a anisotropia, atingindo resistência à tração média de 1650 MPa. A análise microestrutural revelou matriz martensítica com austenite revertida e endurecimento por precipitação.

Os resultados demonstram que a combinação entre a otimização dos parâmetros de deposição e o tratamento térmico de envelhecimento padrão permite produzir componentes de aço maraging de elevado desempenho pelo processo DED-Arc.

Palavas chave: *DED-Arc*, *Aço Maraging,* parâmetros de deposição, tratamentos térmicos, *DoE*

CONTENTS

LIST OF FIGURES

LIST OF TABLES

ACRONYMS

AM	Additive Manufacturing
AISI	American Iron and Steel Institute
ASI	Arc Stability Index
Ar	Argon
BJ	Binder Jetting
BS	British Standards
CMT	Cold Metal Transfer
CTWD	Contact tip to work distance
DED	Directed Energy Deposition
DIN	Deutsches Institut für Normung
El	Elongation
f	Forging Frequency
FS	Forging Steps
GMAW	Gas Metal Arc Welding
GTAW	Gas Tungsten Arc Welding
HAZ	Heat Affected Zone
ISO	Internacional Organization for Standardization
LSC	Low Spatter Control

PBF	Powder Bed Fusion
PAW	Plasma Arc Welding
PS	Pulsed Synergic
SLM	Selective Laser Melting
SL	Sheet Lamination
SR	Solidification Rate
TG	Temperature Gradient
TS	Travel Speed
TRIP	Transformation Induced Plasticity
UTS	Ultimate Tensile Strength
V	Voltage
WAAM	Wire Arc Additive Manufacturing
WFS	Wire Feed Speed
YS	Yield Strength

1 INTRODUCTION

1.1 Motivation

Additive Manufacturing (AM) has been revolutionizing the manufacturing industry, introducing a new way to produce components. This technology, compared to conventional processes, allows shorter production time, greater design freedom and reduction of waste material, in specific applications, this is not universally true across all manufacturing scenarios.

Directed Energy Deposition (DED) has gained prominence for producing large scale components, due to its high deposition rate and lower operational costs compared to other additive manufacturing technologies such as Powder Bed Fusion (PBF).

UTP A 702 is a promising material for DED application, this maraging steel offers high mechanical strength, toughness and good response to heat treatments, making it ideal for military, aerospace and mold industries. Despite these advantages, high alloy steels, including maraging steels, are generally sensitive to thermal cycles which leads to microstructural inhomogeneities and variations in mechanical properties. To ensure DED-produced maraging steels achieve the performance levels required for industrial applications these challenges need to be addressed.

Post-processing heat treatments are essential in maraging steels to induce precipitation hardening and achieve maximum strength. However, these treatments do not eliminate microstructural or compositional inhomogeneities inherent to the DED process, nevertheless, is relevant to study this post-processing aging treatment because of the material´s strengthening mechanism.

Considering the demand for maraging steels, by advancing knowledge in this field DED can become a competitive alternative to conventional manufacturing methods of maraging steels, paving the way for more efficient industrial production.

1.2 Objectives

This thesis aims to investigate the Directed Energy Deposition Arc (DED-Arc) for the fabrication of Maraging steel UTP A 702, with a particular emphasis on optimizing deposition parameters through a statistical Design of Experiments (DoE) methodology. The optimization focuses on enhancing process stability and reliability, which are critical for achieving consistent and defect free components.

Following the deposition process, a post-processing aging heat treatment is applied to evaluate its influence on the microstructure and mechanical properties of the fabricated samples. The characterization of the material, both in the deposited and aged conditions, is carried out through uniaxial tensile testing, optical microscopy, and fractographic analysis. These methods aim to determine the suitability of the applied heat treatment and assess the overall feasibility of producing high-performance UTP A 702 components via DED-Arc.

1.3 Document organization

The document is organized in the following way:

- Chapter 1 - Abords the motivation that led to the development of this work and the goals that we intend to achieve.
- Chapter 2 - The result of the literature review, with focus on DED of Maraging steels and heat treatments.
- Chapter 3 - Describes the material used, experimental procedure and methodology.
- Chapter 4 - Presents and discusses the experimental results, including response surface analysis, statistical evaluation (ANOVA), optimization of deposition process parameters and concludes with the mechanical and microstructural characterization of the produced samples.
- Chapter 5 - Presents the key findings of this study and proposes directions for future research.

2 FUNDAMENTALS AND LITERATURE REVIEW

2.1 Additive Manufacturing

Additive Manufacturing (AM) technologies have become a prominent topic in the manufacturing and engineering sectors, such as the automotive, aerospace, defense and medical industries [1]. Unlike traditional manufacturing, AM forms components through a layer-by-layer deposition process, where materials are heated to a molten state and deposited along a predetermined path to achieve the desired shape [2].

The major advantage of additive manufacturing is its ability to produce complex shaped parts with high accuracy without relying on cutting tools, fixtures, dies, or the complex processes required by traditional machining, allowing the conservation of raw materials and reducing processing cycles [3]. Additionally, its manufacturing process can be adjusted as needed enabling its automation, conceptualization, and distribution[2].

However, AM still faces limitations, from both technological and economic points of view. Challenges like surface finishing, the build space of the machines (particularly relevant to PBF), the high marginal cost of production and in, some technologies, the quality of the produced parts [4].

Initially, AM was primarily used to produce prototypes for validating aesthetic aspects and later for testing the functionality of parts [4]. However, breakthroughs in both the process and the materials used have expanded its applications, enhancing the quality and functionality of the parts produced [5]. Although, AM research focuses on fabricating complex-shaped metal parts, particularly using materials that are difficult to process, in industrial applications it is involved in the production of relatively simple shapes [4].

To standardize terminology, AM technology is categorized into various types based on the heat source and the methods of material supply [2]. The Table 2.1 presents the seven categories for AM technologies according to the ISO/ASTM 52900:2021 standard [6].

Table 2.1 - Additive manufacturing process categories according to ISO 52900:2021 [6]

Categories	Definition
Binder Jetting	Process in which a liquid bonding agent is selectively deposited to join powder materials
Directed Energy Deposition	Process in which focused thermal energy is used to fuse materials by melting as they are being
Material Extrusion	Process in which material is selectively dispensed through a nozzle or orifice
Material Jetting	Process in which droplets of feedstock material are selectively deposited
Powder Bed Fusion	Process in which thermal energy selectively fuses regions of a powder bed
Sheet Lamination	Process in which sheets of material are bonded to form a part
Vat Photopolymerization	Process in which liquid photopolymer in a vat is selectively cured by light-activated polymerization

2.2 Additive Manufacturing of Metals

The additive manufacturing of metals can be classified into four categories, as presented in the Figure 2.1 [3]. This classification considers the type of deposited material.

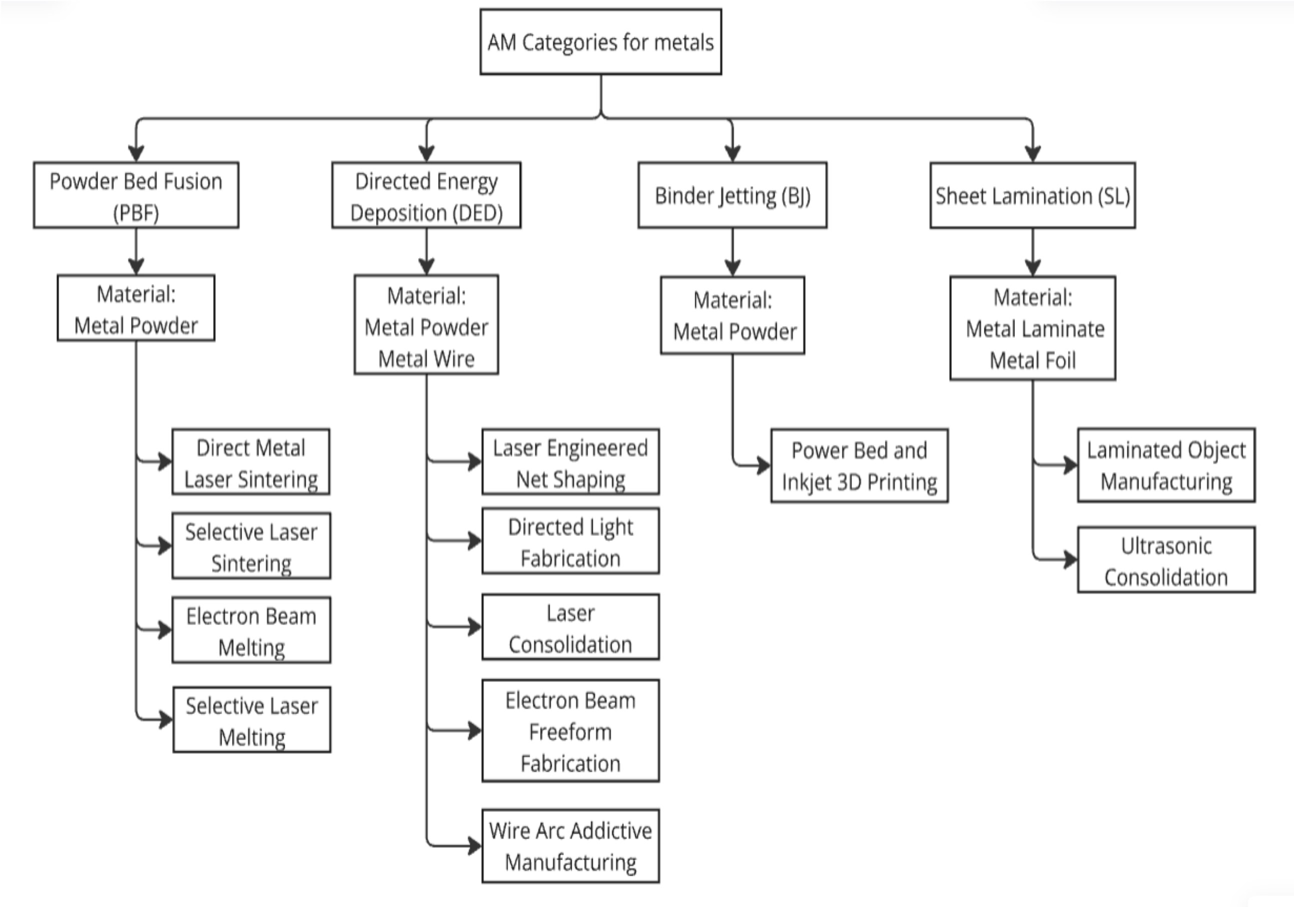

Figure 2.1 - Categories of AM for metal materials [3]

Powder Bed Fusion (PBF) and Directed Energy Deposition (DED) are the most notable among these categories. PBF processes can produce components with high geometrical accuracy, but with expensive equipment, materials, operation costs and lower building rates when compared to other metal AM processes. Furthermore, the material used is metal powder, which poses health risks to workers requires a system to control the hazardous environment [3]. Additionally, the process is prone to the formation of defects such as pores, which can compromise the structural integrity of the parts [5].

DED utilizes a laser, electron beam, or electric arc to generate a melt pool into which feedstock material is continuously supplied. For laser and electron beam systems, material transfer occurs via surface tension and melt pool bridging, rather than discrete droplet formation. Compared to PBF it has lower resolution and it also requires post machining, but it achieves a higher material deposition rate and is more cost effective to produce large metallic components. Moreover, if metal wire is used as feedstock rather than metal powder, we eliminate the need for a recycling system and reduce the raw materials cost, as show in Table 2.2 [3].

Table 2.2 - Approximate cost of different metal materials in wire and in powder, in 2015 [3]

Feedstock	Ti-6Al-4V	Inconel 718	Inconel 625	Stainless Steel 316L
Wire (€/kg)	144	70	59	14
Powder (€/kg)	336	96	96	48

Other additive manufacturing processes, such as binder jetting (BJ), uses a water-based liquid binder that is added to the powder to form layers, besides metals it can handle a wide variety of polymers. It still faces challenges related to the strength and final density of the part, requiring post-process treatments to improve mechanical properties [7].

The Sheet Lamination (SL) process combines additive and subtractive techniques to create parts layer by layer, these layers are joined by a thermal adhesive, through the application of heat and pressure. This technology has several advantages, such as low cost, no need for post processing or support structures, no thermal deformation and can produce large parts. However, this method leads to waste of material, poor surface resolution and difficulty in creating internal cavities [7].

Since Directed Energy Deposition (DED) enables the reduction of waste, the production of complex geometries without an increase in costs and doesn't require tooling, becoming a viable option for the industry [8]. The use of an electric arc as a heat source attracts more attention, due to the efficiency and cost advantages when compared to other heat sources previously mentioned. Economically, when arc power is used as the heat source, its cost is typically around 1/10 of a laser transmitter and 1/30 of an electron beam generator. From the point of view of efficiency, laser-based AM are not a good choice to produce high reflectivity metal alloys, since a laser has a low energy absorption rate and electron beam-based AM needs to work in a vacuum space, limiting the product size and increasing the difficulty of operation [3].

2.3 Directed Energy Deposition-Arc

2.3.1 Process Fundamentals

Directed Energy Deposition-Arc (DED-Arc) employs an electric arc as the heat source and solid wire as the feedstock material, it is commonly referred as WAAM (Wire Arc Additive Manufacturing) within the scientific community [9]. This method sacrifices precision and geometric complexity compared to laser-based powder additive manufacturing, but offers broader applications, lower costs, and the capability to produce large parts. Moreover, it enhances raw material utilization and reduces the product manufacturing cycle [8]. It can deposit titanium-, nickel-, and iron-based materials, besides stainless steel with a high deposition rate, compared to other AM processes [10].

This AM technology has evolved from traditional welding processes, including deposition welding, relying on fundamental concepts of automatized or robotized welding processes. DED-Arc can be characterized based on the heat source into Gas Tungsten Arc Welding (GTAW), Gas Metal Arc Welding (GMAW), and Plasma Arc Welding (PAW) [11]. Figure 2.2 shows these processes, the gas supplied is Argon.

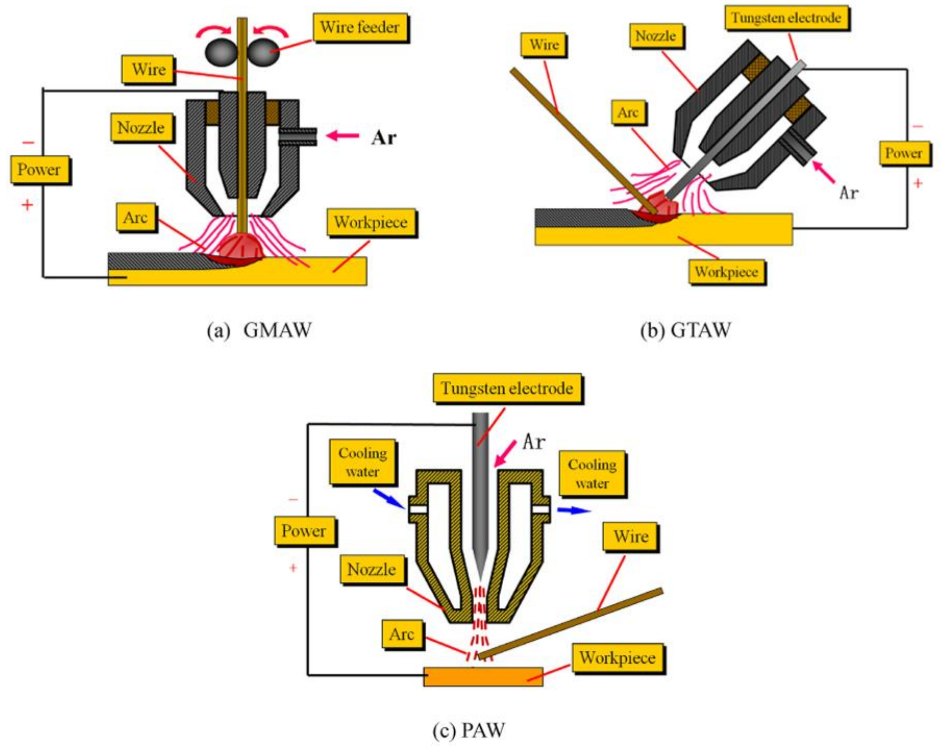

Figure 2.2 - Fundamental features of GMAW, GTAW and PAW processes [3]

Gas Metal Arc Welding (GMAW), is the most used process in DED-Arc, it is a fusion-based arc welding process where the arc is established between the tip of a consumable wire and the workpiece under the protection of an inert or active shielding gas that also protects the weld pool and adjacent material [5], an automatic feeding system is incorporated to transport the consumable metal wire, which is typically positioned perpendicular to the substrate. GMAW offers high melting efficiency and deposition rates, that range from 15 to 160 g/min and can weld the most commercially important metals, including copper, aluminum, and stainless steel. However, GMAW-based DED-Arc usually suffers from poor arc stability [3], and generates weld fumes and spatter due to the electric current passing through the feedstock [9].

Gas Tungsten Arc Welding (GTAW) produces high-quality welds by using an open arc between a non-consumable tungsten electrode and the workpiece. It generates no slag or spatter, requires minimal post-weld cleaning, and can be easily applied in all welding positions [3], but the deposition rates are significantly lower that GMAW-based DED-Arc [9]. Plasma Arc Welding (PAW) is similar to GTAW, but its arc is constrained by a nozzle, resulting in a more focused arc. This increases arc stability, improves heat transfer efficiency, and enhances welding speeds [3]. The Heat Affected Zone (HAZ) of PAW beads is narrow and thin, allowing for better control of the weld geometry [5], it can also weld most refractory metals used in industrial applications [3].

GTAW-based and PAW-based systems require a separate wire feed system, which allows for flexible wire feed directions and positions, such as back feeding, side feeding, and front feeding. On the other hand, in GMAW-based systems, the welding torch and wire are coaxial, simplifying path generation and robot programming [3].

In the pursuit of a more stable process, a variant of GMAW, known as cold metal transfer (CMT) has developed. It is an advanced material transfer process, with a deposition type based on a short circuit, that controls molten metal deposition, with reduced heat input, in which an incorporated control system detects when the electrode wire tip contacts the molten pool and, using a servomotor, retracts the wire in a push-pull electromechanical process, to control the droplet transfer, nevertheless, GTAW and PAW offer higher arc stability due to their controlled energy input and arc characteristics [5]. CMT offers advantages such as reduced spatter and lower heat input, making it suitable for thin-walled components. However, for thicker sections, CMT may be prone to lack of fusion defects, and its applicability must be evaluated case-by-case [3].

2.3.2 Process Parameters and Deposition Strategies

This section addresses the process parameters that significantly impact the properties of components manufactured by DED-Arc. To fully optimize the utilization of a manufacturing process a meticulous selection and implementation of a combination of process parameters and deposition strategies need to be addressed [12].

In GMAW, the process parameters that significantly affect the outcome are wire diameter, wire feed speed (WFS), travel speed (TS), arc current and voltage (V), contact tip to work distance (CTWD), shielding gas and torch angle [12], the effect of the parameters are presented in Table 2.3.

The characteristics and the quality of the deposited structure are directly related to the heat input. As excessive heat input results in the remelting of the layers previously deposited, deteriorating the macrostructure and bead geometry, on the other hand, low heat input ensures a uniform deposition and reduces porosity, by lowering the droplet temperature and gas solubility in the melt pool, however in the case of thick components, higher heat input may be necessary to ensure proper fusion and avoid defects [13]. Heat input also influences the melt pool size, with lower values producing smaller width-to-height ratios due to the rapid solidification, while higher values increase fluidity and, consequently, the molten pool extension. The process parameters that influence the heat input are arc current, arc voltage and travel speed (TS), with studies showing that the WFS/TS is the most critical parameter when controlling heat input. Additionally, variations in the heat input induce changes in the microstructure [14].

Table 2.3 - Relationship matrix between parameters and the finished product performance (adapted from [12])

Parameters \ Performance	Structural Integrity	Surface Finish	Substrate Warping	Residual Stress	Porosity	Cracks	Hump
Type of Heat Source	Strong	Weak	No effect	No effect	Strong	No effect	Strong
Type of Wire Material	Strong	Strong	Strong	Weak	Strong	Strong	No effect
Wire Feed Speed	Strong	Strong	Strong	Strong	Strong	Strong	Weak
Travel Speed	Strong	Strong	No effect	No effect	Weak	Strong	Strong
Voltage (V)	Strong	Strong	Strong	Strong	Strong	Strong	No effect
Current (A)	Strong	Strong	Strong	Strong	Strong	Strong	Strong

The welding shielding gas is an important parameter, since it affects bead geometry, process stability, transfer mode and weld appearance [15]. It is typically supplied through the welding torch, allowing the protection of the molten material from contamination, preventing defects such as cracking, porosity, inclusions and the formation of oxides. Gas composition significantly influences the process, it impacts the microstructure of components and the stability of the welding arc. In reactive materials, insufficient oxide in the melt pool can cause arc wandering, because the arc shifts towards the substrate to locate new oxides, leaving a sputtering zone. To address this challenge an oxidizing-doped shielding gas is used, allowing an increased travel speed, improved penetration and a reduced surface tension of the molten metal [13]. The flow rate is another critical factor, a higher flow rate leads to poor penetration due to turbulence, which also traps atmospheric gases resulting in the increase of the porosity on the final part. Recent innovations, such as inert chambers and flexible tent shielding were introduced to manage turbulence, enhance surface finish and deposition efficiency [12].

The type of wire is a crucial factor thar affects the structural integrity and quality of the parts produced. The wire diameter plays a significant role in determining the heat input, deposition rate, overall quality of the deposited bead and the width of the molten pool. Moreover, the quality of the wire is critical, variations in wire size, imperfections or defects can lead to voids or porosity [12].

Key welding parameters (introduced previously) are directly related to arc stability, making it a critical factor in achieving high-quality parts, as it governs the consistency of metal transfer, bead formation and overall weld integrity. Stable arcs ensure uniform heat input, controlled droplet detachment and reduced spatter, essential for process efficiency and defect prevention [16].

Moreover, a crucial aspect to manufacturing suitable parts, made by DED-Arc, lies is the design of an efficient deposition strategy. For single-pass multilayer deposits, toolpath planning is critical, a unidirectional toolpath causes material accumulation at starting points, whereas bidirectional balances deposition and uneven material deposition. Combinations of wire feed speed and travel speed can also mitigate material defects in unidirectional deposition [12]. In multi-layer and multi-bead deposits, proper overlap distances (hatch distance) are essential to avoid defects like valleys between beads, geometry accuracy and good surface finish [15]. So, deposition strategies like oscillation, parallel and weaving are implemented, as illustrated in Figure 2.3.

These strategies define the toolpath, the start and end positions for each layer, inter layer waiting time and heat management [17]. The oscillation strategy causes excessive heat buildup, leading to shrinkage, oxide formation, element loss, and gas trapping. The parallel strategy reduces heat accumulation by letting adjacent beads cool as the torch alternates positions. The weaving strategy combines parallel deposition with a linear weave, creating wider, flatter beads instead of tall, narrow ones. To achieve a uniform single-pass bead, precise torch programming is required [17].

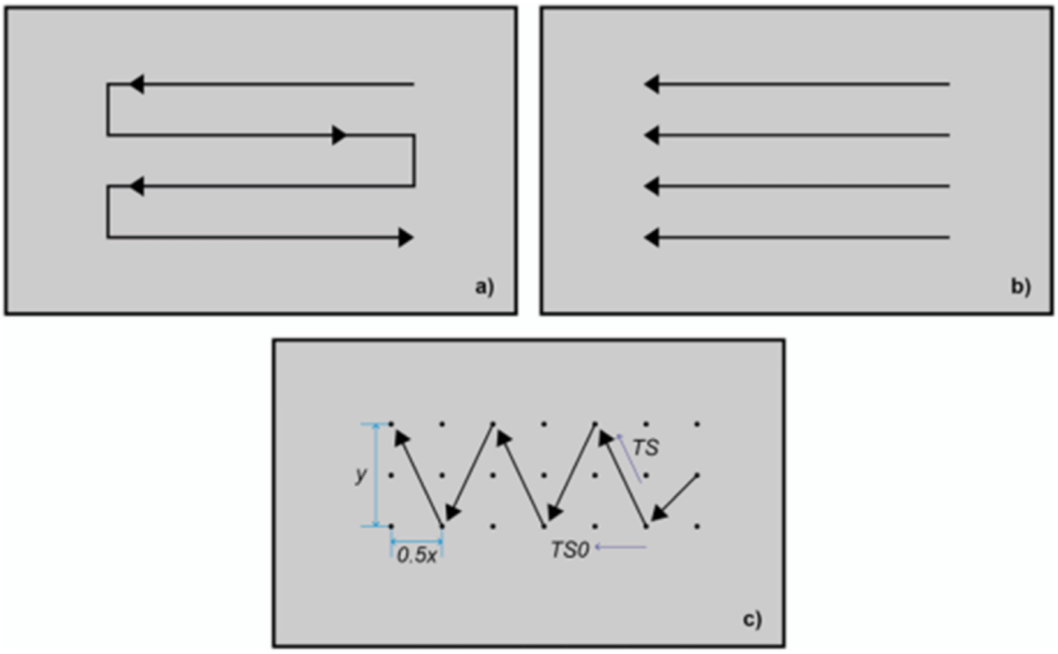

Figure 2.3 - Deposition Strategies: a) Oscillation, b) Parallel, c) Weaving [12]

In DED-Arc, metal transfer occurs mainly through three conventional modes: spray, globular and short-circuit [18], but more advanced deposition modes are utilized, for tool steels DED-Arc processes are CMT, low spatter control (LSC) and pulsed synergic (PS). The CMT process has already been presented in section 2.3.1. LSC is a dip transfer process based on short-circuit, this is, just before breaking the short circuit bridge the current is reduced, which causes high arc stability and low spatter generation [18], [19]. The waveform of CMT and LSC process can be observed in Figure 2.4.

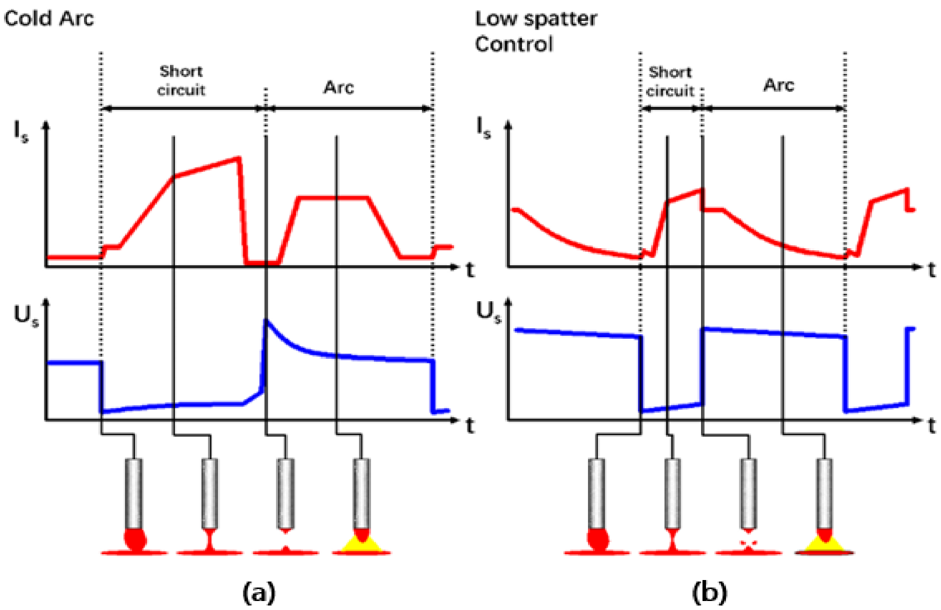

Figure 2.4 - Waveform of a) CMT and b) LSC [20]

The PS uses lower average current, due to the current pulse. During the lower period the current pulse is kept at lower levels to keep the wire material, but maintaining the electric arc, then the peak current is increased above the transition current to promote the transfer of a metal drop that is shed in the phase where the current is lowered [21], as presented in Figure 2.5.

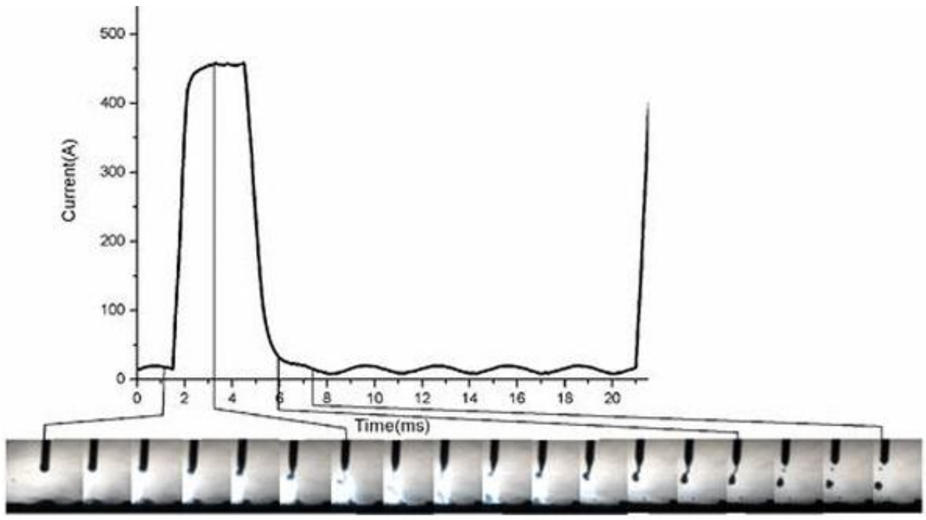

Figure 2.5 - The shape of the current and droplet in pulsed transfer mode [4]

A study showed that additive manufacturing of AISI H13 steel, a hot work tool steel, via DED-Arc was viable using CMT, LSC, and PS modes, all producing defect-free deposits. LSC and CMT exhibited similar arc voltage and current values, while PS displayed oscillations, resulting in lower current and higher voltage. Among the modes, LSC had the lowest energy consumption, PS generated the highest substrate temperatures and deposited the least metal, and CMT produced the largest deposit dimensions [19].

2.4 Direct Energy Deposition - Arc of Maraging Steels

Due to the lack of information about the material in study, UTP A 702. This section focuses on Maraging Steels because of the similar mechanical properties and chemical composition [22], [23]. Information about the material in study is presented in section 3.1 .

2.4.1 Process Overview

In a previous study [24], has used a filling material of 18Ni (350) Maraging Steel as a wire with a diameter of 1.2 mm. It was manufactured with a thin wall part 160 mm in length, 90 mm in height and 9 mm in thickness by GMAW-based DED-Arc. The optimized process parameters were as follows in Table 2.4. To ensure that the height at both ends of the wall were equal, an alternating direction deposition mode and an elevation of 2.0 mm of the torch after the deposition each layer was used. The temperature between layers was controlled at 150 ºC (± 10ºC) though air cooling. The shielding gas used was pure Argon (Ar) with a flow rate of 25 L/min.

Table 2.4 - Process Parameters [24]

Current (A)	Travel speed (mm/s)	Wire Feed Speed (m/min)	Heat Input (J/cm)
133	3.5	4.2	7980

2.4.2 Microstructure

The microstructure of metals is the arrangement and organization of phases, grains, and precipitates at the microscopic level, which directly affects the mechanical and behavioral properties of materials [5]. The microstructure of metals processed by DED-Arc is significantly influenced by variations in thermal cycles and process parameters, changing the solid phase transformations and grain morphology. To optimize the production of Maraging steels via DED-Arc, it is essential to understand their solidification behavior and phase transformations, which differ from other alloys due to their unique precipitation hardening mechanism [11].

In steel components fabricated by DED-Arc, the microstructure differs from those produced by conventional methods, with DED parts consisting predominantly of low-angle columnar grains due to the large heat input and slow cooling rates during layer deposition. The high thermal gradients and interlayer heat accumulation can lead to the formation of oxide inclusions, while solidification occurs entirely in the austenitic mode. Upon cooling, a portion of this austenite transforms into lath martensite, whereas some retained austenite remains at room temperature due to local variations in composition and cooling rate [25].

The grain structure is strongly influenced by the thermal gradient and build direction, The main factors that influence cooling are the solidification rate (SR) and the local temperature gradient (TG). A higher TG/SR ratio leads to the formation of columnar crystals, while a lower one leads to the formation of equiaxed grains [2], [11].

However, even for grains with the same crystal structure, their morphology, orientation and size may vary, due to the thermal history of the process. As presented in Figure 2.6, this heterogeneity in the microstructure of maraging steel is evident along the build height. It originates from the high heat input and repeated reheating between layers, which govern the local solidification rate and the extent of epitaxial growth from previously deposited material. Solidification occurs entirely in the austenitic mode, with epitaxial columnar grains growing along the primary heat extraction direction. During subsequent cooling, most of the austenite transforms into lath martensite, while a small fraction remains as retained austenite due to nickel enrichment and the relatively slow cooling rates inherent to the DED-Arc process [25], [26].

In the bottom and middle regions, repeated reheating promotes epitaxial grain growth and partial remelting, producing coarse columnar grains and inter-dendritic segregation of alloying elements such as Ni, Mo, and Ti. These regions consequently exhibit a higher fraction of retained austenite and a coarser microstructure. In contrast, the top region, which solidifies directly without subsequent reheating, develops a finer cellular or dendritic morphology with lower austenite content. This vertical gradient in grain size and phase distribution, clearly illustrated in Figure 2.6, is characteristic of the DED-Arc process and has been consistently reported for 18Ni maraging steels [11], [25]. Therefore, the resulting deposited microstructure consists predominantly of lath martensite, with smaller fractions of retained austenite and fine intermetallic precipitates. These features distinguish DED-Arc maraging steels from conventionally processed counterparts, which typically exhibit a more homogeneous microstructure after heat treatment [27].

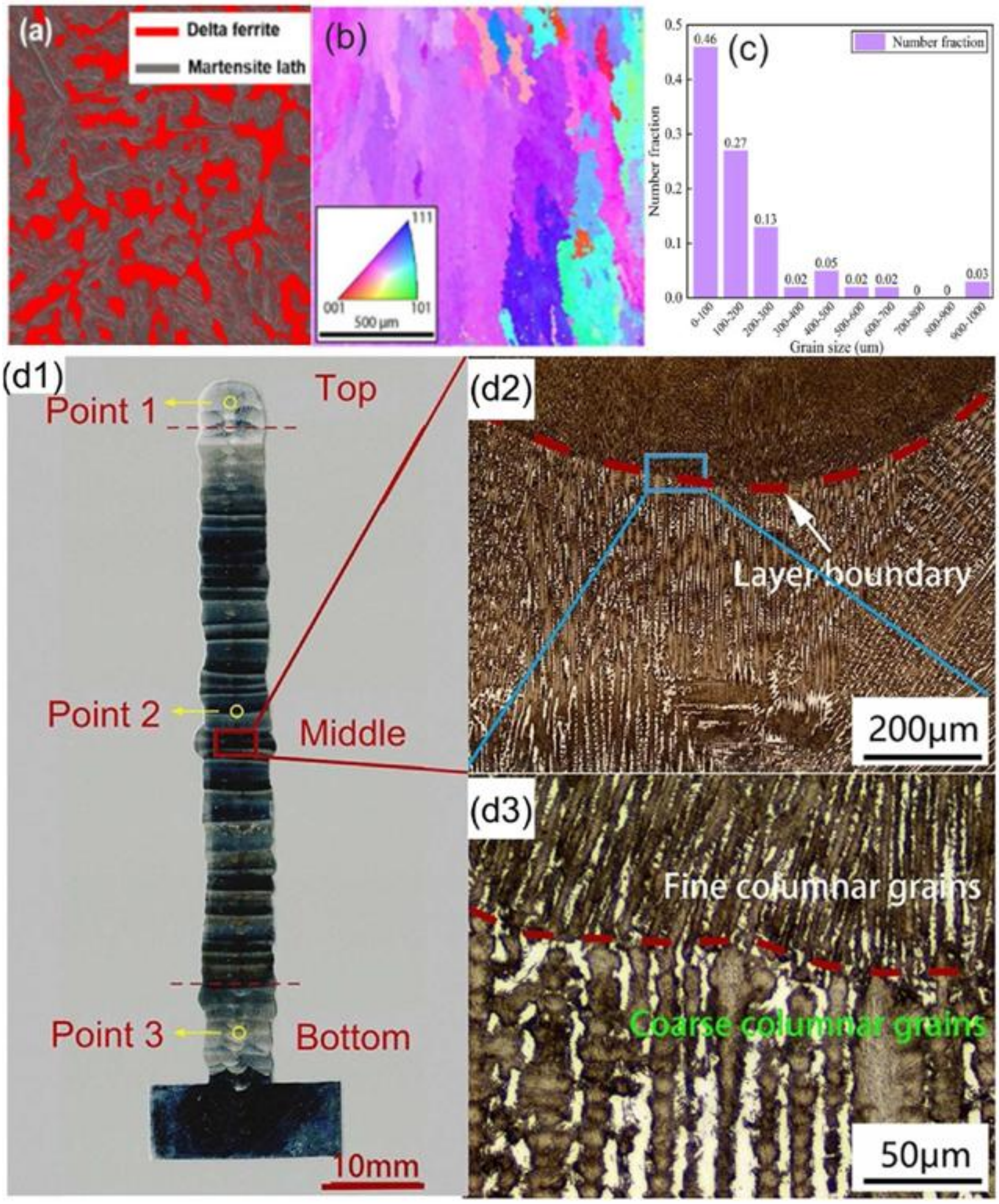

Figure 2.6 - The morphology, orientation and size of grains of DED-Arc maraging steel, (a) grain morphology, (b) grain orientation, (c) grain size, (d1) macroscopic morphology, (d2) low magnification of middle region, (d3) high magnification view of the layer boundary [11]

Despite the growing number of studies addressing the relationship between processing parameters, microstructure, and mechanical performance, there is still a lack of literature on the Direct Energy Optimization (DEO) principles and their specific application to DED processes. This gap limits the systematic understanding and optimization of process variables that govern heat input, thermal gradients, and subsequent microstructural evolution.

2.4.3 Mechanical Properties

Components produced through Directed Energy Deposition with Arc (DED-Arc) exhibit a heterogeneous microstructure, which promotes anisotropy in their mechanical response. Wang et al. [27] investigated the fabrication of 18Ni (350) maraging steel using DED-Arc and reported pronounced directional dependence of mechanical properties. The as-deposited specimens demonstrated higher ultimate tensile strength and yield strength along the build direction compared to the horizontal orientation. This anisotropic behavior was attributed to the alignment of elongated columnar grains and to local chemical segregation retained within the lath martensitic microstructure. Consequently, such microstructural features significantly influence hardness, ductility, and the overall mechanical performance of DED-Arc fabricated parts. The mechanical properties of the 18Ni (350) is represented in the Figure 2.7.

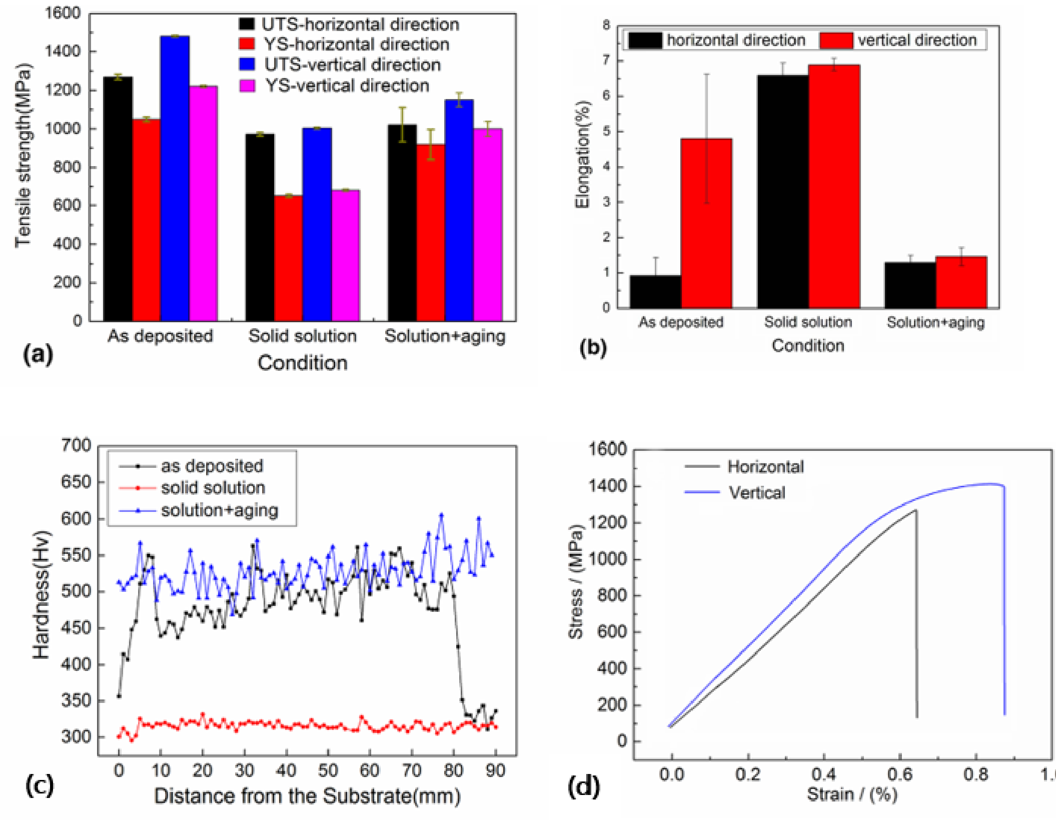

Figure 2.7 - Mechanical properties of 18Ni (350) maraging steel fabricated by DED-Arc under different heat treatments: (a) Tensile and Yield Strength; (b) Elongation; (c) Vickers Hardness; (d) Stress - Strain curves (as-deposited) [27]

Despite the growing number of studies addressing the relationship between processing parameters, microstructure, and mechanical performance, there is still a lack of literature on the Direct Energy Optimization (DEO) principles and their specific application to DED processes.

This gap limits the systematic understanding and optimization of process variables that govern heat input, thermal gradients, and subsequent microstructural evolution.

To mitigate anisotropy and improve homogeneity, studies have investigated post-deposition heat treatments and thermomechanical strategies such as inter-pass rolling and hot forging, as discussed in chapter 2.5 and chapter 2.6.

2.4.4 Defects

The DED process presents similar defects to those observed in conventional welding, such as porosities, lack of interlayer adhesion, cracks, delamination, residual stress and distortions [28].

The successive expansion and contraction from thermal cycles causes the accumulation of residual stress remaining in the part after cooling and can lead to distortions. Affecting the materials mechanical strength and dimensional accuracy. The optimization of deposition parameters and deposition strategies, such as starting the deposition from the outside and ending at the center, helps minimize this defect. When the accumulation of residual stress between layers exceeds the materials yield strength or chemical variations during solidification, it can lead to the formation of cracks. Delamination, on the other hand, results from partial fusion between layers or inadequate thermal control. These two defects can be mitigated with the preheating of the substrate, adjusting heat input and the use of contamination free materials. The contamination of the material and the absorption of atmospheric gases, particularly hydrogen, leads to the formation of porosities during solidification, negatively impacting the mechanical properties. Proper cleaning of the feedstock and correct use of shielding gas are essential to reduce porosity, process parameters like WFS and TS have minimal influence [28], [29].

The presence of these defects in maraging steels, as observed in the Figure 2.8, result in a brittle fracture mode characterized by cleavage fracture and intergranular cracking. The presence of these brittle fracture features suggests a weak grain boundary cohesion, due to elemental segregation or insufficient diffusion between layers. In the section 2.6 the changes on defects after heat-treatments are addressed [27]. Another approach to minimizing defects in DED is the use of the Hot Forging variant, which applies forging in the fusion zone, promoting pore collapse and reducing their severity [28].

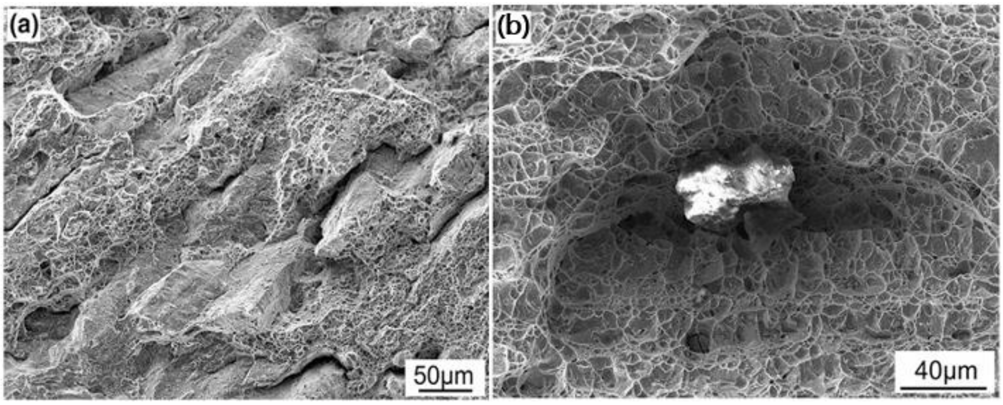

Figure 2.8 - Typical defects on the fracture surface of the as-deposited maraging steel: a) Crack; b) Oxide Inclusions [27]

2.5 Process Variants

Parts made by DED, experience significant residual stresses, deformations, large grain sizes and anisotropy, to address these issues post processes are employed [11].

2.5.1 Interpass cold rolling and hot forging

Cold rolling consists of the use of a rolling machine to apply loads to plasticly deform the deposited structure, while the sample is clamped in a rigid structure. As each new layer is deposited, it is allowed to cool to room temperature before being rolled at high pressure. This process induces local plastic deformation, which in turn increases the dislocation density and a significant reduction in grain size [11]. The reheating of the rolled layer in the subsequent layer deposition also induces grain refinement [13]. The temperature during the rolling process, is an important factor, the residual heat of the component in the forming process promotes elongation of the material due to the thermal connectivity, which is conducive to improving the flatness and surface roughness of the weld surface and increasing productivity [11].

Following the process of rolling surges the hot forging, it consists of a hammer placed inside the gas nozzle, which is activated by vibrating actuator, operated electromagnetically or mechanically, as illustrated in Figure 2.9. It is designed to utilize the viscoplastic deformation of materials at high temperatures to increase strength, reduce residual stress, refine the microstructure and close voids [13], [30].

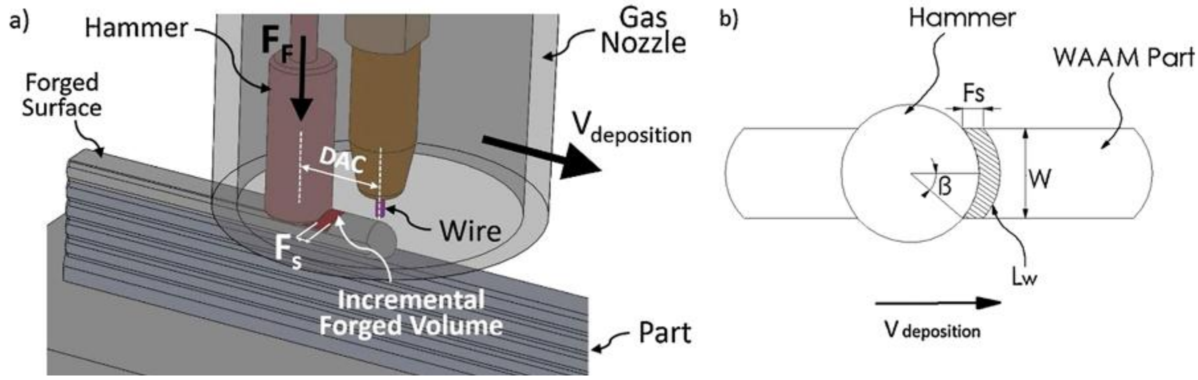

Figure 2.9 - Schematic representation of forging area in HF-WAAM: (a) isometric (3D); (b) top view (2D) [13]

The position and geometry of the vibrating hammer has more than one alternative, such as a hammer with circular geometry positioned outside the torch, a hammer with a circular crown geometry or using the external cylinder protecting the torch as a hammer [31].

The Table 2.5 shows the process parameters necessary to parameterize this process in an efficient way.

Table 2.5 - Hot Forging Parameters [31]

Parameters	Forging force (N)	Forging Frequency (Hz)	Forging Step (mm/cycle)	Distance from the hammer axis to the electric arc (mm)

There is a relation between the forging step, FS, forging frequency, f, and Travel Speed, TS, equation 2.1. If this relationship is not met, areas of deposited material may remain without proper forging [31].

$$\boldsymbol{FS = \frac{60\ \times TS}{f}\left[\frac{mm}{ciclo}\right]} \qquad \textbf{2.1}$$

Duarte et al. [32] investigated the use of *in-situ* hot forging on a part of CuAL8 Alloy fabricated by DED. The hot forging system developed in this study features a pneumatic actuator with a circular hammer, that deforms the material after the deposition. This process operates at high temperatures, approximately 750 ºC, allowing for dynamic recrystallization, which refines the grain structure and improves isotropy. This research demonstrates that hot forging is a superior alternative to cold rolling, since it enables the refinement of the microstructure, enables recrystallization and stress relief without the limitations of cold rolling, such as requiring high loads, excessive strain hardening or crack formation.

2.6 Heat Treatments

Post-process heat treatments have a wide role DED-Arc in enhancing material strength, reducing residual stress and improving the microstructure. The choice of heat treatment is dependent on the material, manufacturing process, working temperature and heat treatment conditions [11].

Solution annealing is a key step in the heat treatment of maraging steels, particularly for those produced by additive manufacturing, as it eliminates chemical segregation and restores a uniform martensitic structure. Studies by Kan et al. [33] and Conde et al. [34] demonstrated that heating the alloy to temperatures above the Ac_3 point results in complete austenitization, which dissolves segregation of alloying elements such as Ni, Ti, and Mo that form during solidification. Upon cooling, this homogeneous austenitic phase transforms into a fine, uniform martensitic matrix. Kan et al. showed that a treatment at 840 °C for one hour followed by air cooling effectively removed inter-dendritic and cellular segregation, promoted recrystallization into equiaxed prior-austenite grains, and reduced retained austenite to less than 3%. However, also noted that such extensive homogenization reduces the solute enrichment responsible for stabilizing austenite, leading to a predominantly martensitic structure after cooling. Overall, the literature indicates that solution annealing above Ac_3 is essential for achieving a homogeneous and stable martensitic matrix, providing the structural and compositional foundation for subsequent aging or tempering treatments.

During aging heat treatment, the low-carbon lath martensite becomes thinner while the austenite phase increases, transforming from elongated dendritic shapes into more equiaxed structures. This transformation is driven by elemental segregation, which promotes austenite reversion. At the same time, martensite that was not fully stabilized during the solution treatment undergoes a reverse transformation into austenite, further elevating the overall austenite content. Moreover, aging enables the precipitation of strengthening phases, such as Ni_3Ti, Ni_3Mo, and Fe_2Mo, from the martensite matrix, however, in DED-Arc fabricated samples, this precipitation is often non-uniform due to prior thermal cycles and inherent microstructural heterogeneity. Although the aging treatment significantly increases microhardness, the improvements in ultimate tensile strength and yield strength are marginal compared to the as-deposited state. More importantly, the marked reduction in elongation indicates that while the reverse transformation and precipitate formation enhance hardness, they may also lead to embrittlement. Consequently, the modest gains in tensile strength are offset by a substantial loss in ductility, highlighting the need to optimize aging treatments to achieve a more favorable balance of strength and ductility in DED-Arc produced materials [22], [26]. The Figure 2.10 shows this microstructure, after solution annealing and aging.

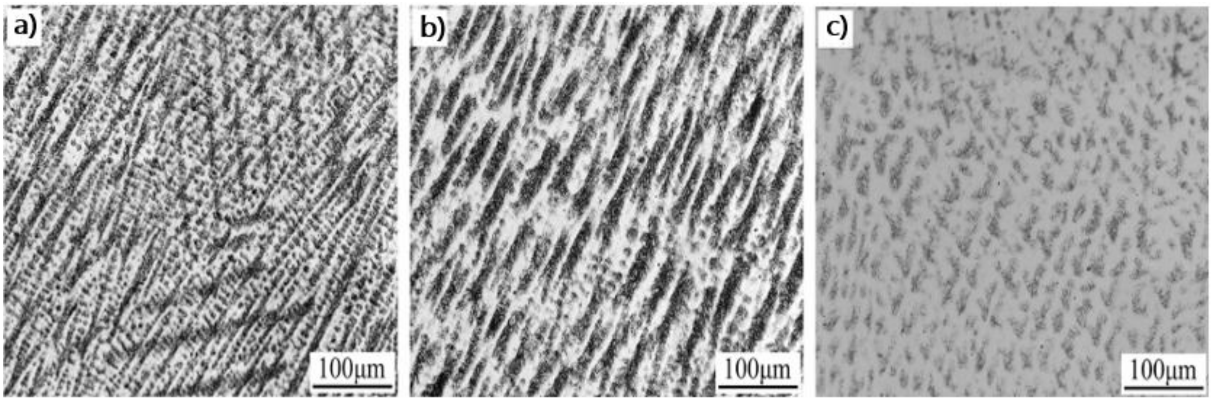

Figure 2.10 - Microstructure of the maraging steel produced by DED-Arc of a solution and aging-treated part, a) Top; b) Middle and c) Bottom region [24]

In a study with maraging 300 steel, a material with similar chemical composition to the UTP A 702 [34], [35], produced via Selective Laser Melting (SLM), has studied in order to understand the martensite to austenite reversion through a solution annealing and isothermal tempering, to improve the ductility and toughness of the produced part. The homogenization treatment was conducted at 820 ºC for one hour, followed by air cooling. During the tempering, the Transformation Induced Plasticity (TRIP) is responsible for inducing the martensite to austenite reversion, this occurs when the material is heated between the Ac1 (temperature at which ferrite starts to transform into austenite) and Ac3. The tempering has performed with a soaking time of 2200 seconds, a 500 ºC/s heating rate, a cooling rate of 5ºC/s and at three different temperatures 610ºC, 650ºC and 690ºC. The study concluded that isothermal tempering at 610ºC to 650ºC offers an optimal balance between austenite formation and thermal stability, as shown in Figure 2.11, with higher temperatures inducing low austenite stability after cooling [34].

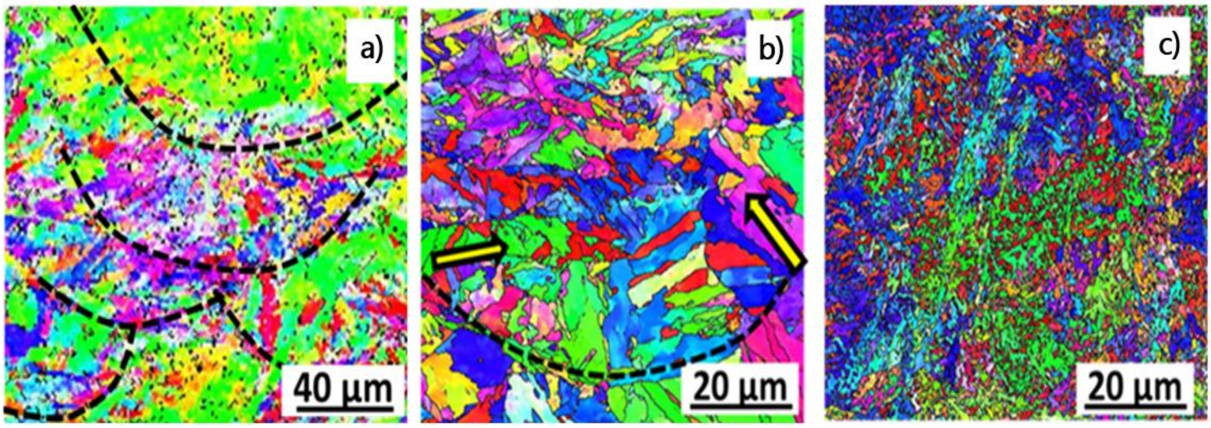

Figure 2.11 - Microstructures of AM maraging 300 steel after: a) SLM deposition, b) homogenization at 820°C for one hour, c) tempering at 610°C [34]

During the annealing treated state, the fracture mode transitions from brittle cleavage to ductile dimple rupture, characterized by the presence of micro-voids that grow forming deep dimples on the fracture surface. After aging, the fracture surface presents shallow dimples alongside cleavage steps indicating a combination of ductile and brittle failure mechanisms. The presence of cleavage steps suggests a localized brittle fracture due to stress concentrations around the hard precipitates [27].

If lower hardness and improved toughness is required, the temperature during the aging temperature can be increased, as represented on Figure 2.12 [36].

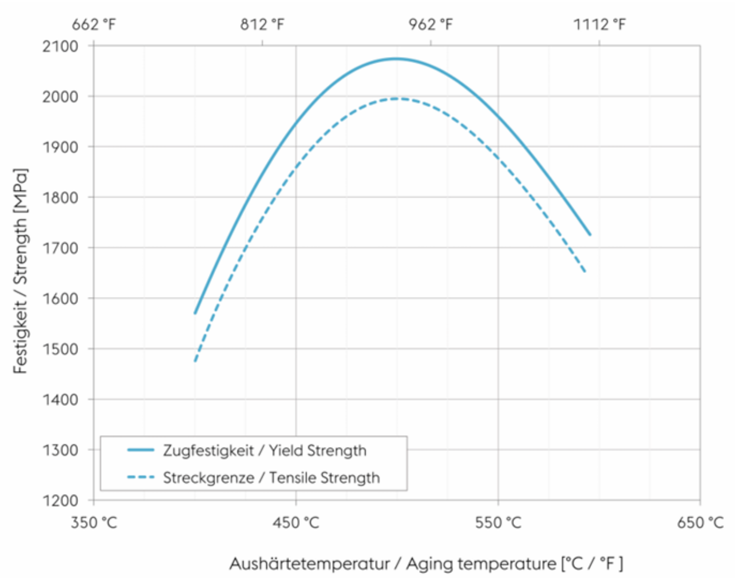

Figure 2.12 - Effect of Aging Temperature on the Hardness of Maraging Steel [36]

3 EXPERIMENTAL PROCEDURE

3.1 Material

The material used was the UTP A 702, a Maraging Steel classified under material number 1.6356 according to EN standards [35]. This material has high strength and toughness, being used for aerospace, military, aeronautical and nuclear industries, besides this it is used to repair and renovate mold parts of high-pressure casting procedures [37], [38] . In the as-deposited state the material is machinable, with the subsequent artificial aging optimizing its strength and hardness, with the following chemical composition expressed in Table 3.1 [35].

Table 3.1 - Chemical composition, in mass percentage of UTP A 702 [35]

C [%]	Al [%]	Mo [%]	Fe [%]	Ni [%]	Co [%]	Ti [%]
0.02	0.1	4.0	Balance	18.0	12.0	1.6

Maraging steels possess unique thermal and physical characteristics that set them apart from conventional high-strength steels. Their high martensite start and finish temperatures allow complete transformation to a soft and ductile martensite upon air cooling, providing good machinability and workability prior to aging. Due to the chemical and metallurgical equivalence between UTP A 702 and 18Ni-350, the standard heat treatment applied to 18Ni-350 was adopted, therefore an aging treatment at a temperature of 480 ºC for 5 hours followed by air cooling was applied [23]. This treatment induces precipitation of nanometric intermetallic compounds (Ni_3Ti, Ni_3Mo, Fe_2Mo), which raises yield strength while maintaining excellent dimensional stability. In addition, maraging steels show protective oxidation behavior, with thin adherent oxide layers forming at intermediate temperatures, and corrosion resistance superior to most low-alloy steels [23], [37].

Although Maraging steel is not a stainless steel, the Schaeffler diagram was used to approximate phase formation due to its widespread application in alloys with similar elements. However, it is important to note that this diagram does not account for solidification modes and only predicts room-temperature microstructures. It predicts the phase formation by evaluating the chromium equivalent ($\mathrm{Cr_{Eq}}$) and nickel equivalent ($\mathrm{Ni_{Eq}}$) of the material composition, representing the effects of alloying elements that promote ferrite and austenite formation, respectively. The Chromium and nickel equivalent are calculated with the equations 3.1 and 3.2 [39].

$$\mathbf{Cr_{Eq}} = \%\mathbf{Cr} + \%\mathbf{Mo} + \mathbf{1.5} \times \%\mathbf{Si} + \mathbf{0.5} \times \%\mathbf{Nb} + \mathbf{2.0} \times \%\mathbf{Ti} \qquad 3.1$$

$$\mathbf{Ni_{Eq}} = \%\mathbf{Ni} + \mathbf{30} \times \%\mathbf{C} + \mathbf{0.5} \times \mathbf{Mn} + \mathbf{30} \times \%\mathbf{N} \qquad 3.2$$

Considering the chemical composition of UTP A 702 in Table 3.1, the $\mathrm{Cr_{Eq}}$ and $\mathrm{Ni_{Eq}}$ are 7,2 % and 18,6 %. In Figure 3.1 can be observed that the expected microstructure is a combination of austenite-martensite.

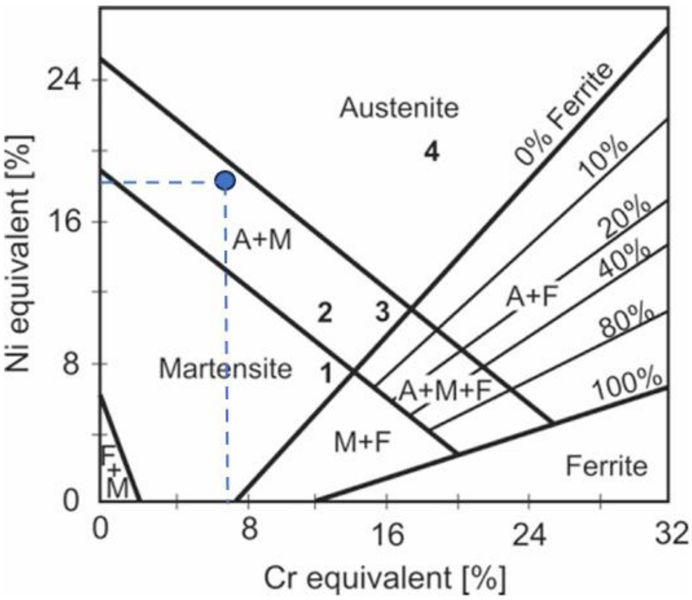

Figure 3.1 - Schaeffler Diagram [40]

3.2 Design of Experiments

With the purpose to optimize the parameters of the DED-Arc process, statistical analysis is used. Being a multi-variable process, a combination of parameters needs to be manipulated effectively, with the goal of minimizing trial-error experiments and enable systematic pre-planning [12]. The Design of Experiments (DoE) methodology is used to estimate the optimal range of process parameters, which is obtained through a mathematical correlation between the process parameters and the deposited single-layer output variables [41].

The response surface methodology (RSM) is a statistical technique that uses multivariate quadratic regression equations to solve multivariate problems, where linear and nonlinear interactions are expected, like DED-Arc. These equations model the functional relationship between process variables and performance or quality measurements. RSM is applied to analyze the impact of independent process variables and their effects on the response and the relation between the independent process variables and the responses are visually represented through three-dimensional surface plots [41].

To generate a quadratic model from a response surface design the central composite design (CCD) method is used. This type of planning consists of a factorial planning 2^k with n_F experiences, 2k axial or star points, n_C center points, being k the number of process variables considered:

- $n_F = 2^k$ points correspond with the vertices of a cube k-dimensional cube, $(x_1, x_2, \ldots, x_k) = (\pm 1, \pm 1, \ldots, \pm 1)$;
- 2k points, designated star points, corresponding with the vertices of a k-dimensional star, $(\pm\alpha, 0, \ldots, 0), (0, \pm\alpha, \ldots, 0), \ldots, (0, 0, \ldots, \pm\alpha)$;
- $n_C \geq 1$ central points, $(x_1, x_2, \ldots, x_k) = (0, 0, \ldots, 0)$;

The total number of experiments is obtained by equation 3.3:

$$N = n_F + 2k + n_C \qquad 3.3$$

The central composite design (CCD) is divided into three types, Circumscribed (CCC), Inscribed (CCI) and Face-Centered (CCF), based on the disposition of the star points as show in Figure 3.2.

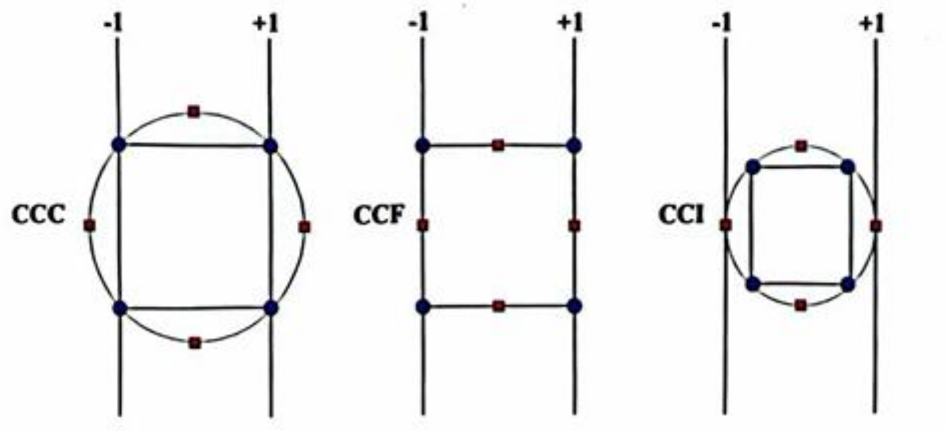

Figure 3.2 - Types of Central Composite Design [42]

For this work the planning used is the Circumscribed Central Composite Design (CCC), because it allows us to address a broader domain of the planning space and is a rotatable planning. The planning is rotatable when the points are rotated relatively to the center and their distribution remains unalterable, leading to more reliable and consistent predictions across the design space [42].

To create the necessary curvature for modeling quadratic responses each factor requires five levels, being $-\alpha, -1, 0, 1, +\alpha$. The distance between the center and the star points is $\pm\alpha$, and is this distance that makes the planning rotatable, α is obtained with equation 3.4 [42].

$$\alpha = (n_F)^{1/4} \tag{3.4}$$

The responses are expressed as mathematical functions, where the process parameters are the constituent factors, as denoted in equation 3.5 [41].

$$Responses = f(x_1, x_2, x_3) \tag{3.5}$$

A second-order polynomial equation is used to represent the response function, assuming that a quadratic regression model can predict the response variable. The equation from the RSM is presented in equation 3.6 . The variable k denotes the number of process variables, β_0 the intercept and β_i, β_{ii} and β_{ij} the coefficients regarding the linear, quadratic and interaction factors, respectively. The $n\beta$ coefficients are estimated with the equation 3.7 [41], [42].

$$Y = \beta_0 + \sum_{i=1}^{k} \beta_i x_i + \sum_{i=1}^{k} \beta_{ii} {x_i}^2 + \sum_{i}^{k} \sum_{j>i}^{k} \beta_{ij} x_i x_j + \varepsilon \tag{3.6}$$

$$n\beta = \frac{(k+1)(k+2)}{2} \tag{3.7}$$

An ANOVA analysis is introduced to the quadratic model to evaluate the statistical significance of response, with the analysis results presented in an ANOVA table (Table 3.2). It begins by calculating the total sum of squares (SST), which measures the overall variation in the data. This total variation is then divided into the sum of squares due to regression (SSR), which quantifies the variation explained by the model, and the sum of squares due to error (SSE), which represents the unexplained variation (Equations 3.8, 3.9 and 3.10) [42]:

$$SST = \sum_{u=1}^{N} (Y_u - \bar{Y})^2 \tag{3.8}$$

$$SSR = \sum_{u=1}^{N} (\hat{Y}_u - \bar{Y})^2 \tag{3.9}$$

$$SSE = \sum_{u=1}^{N} (Y_u - \bar{Y}_u)^2 \tag{3.10}$$

The variables are the observed response value in each experiment Y_u, the arithmetic mean of the responses $\bar{Y}$ and the value predicted by the model $\hat{Y}_u$.

By comparing these components, ANOVA uses the F-test to determine whether the model's predictors have a significant effect on the response variable. The F-value is calculated as the ratio of the mean square regression (MSR) to the mean square error (MSE) (equations 3.11 and 3.12). Under the null hypothesis, where none of the predictors contribute meaningfully, the MSR and MSE are expected to be similar, resulting in an F-value close to 1. However, if the F-value is significantly higher than the critical value from the F-distribution, it suggests that the variability explained by the model is substantially greater than what would be expected by chance, leading to the rejection of the null hypothesis [42].

$$MSR = \frac{SSR}{(\mathrm{n\beta} - 1)} \tag{3.11}$$

$$MSE = \frac{SSE}{N - \mathrm{n\beta}} \tag{3.12}$$

The p-value which ranges from 0 to 1, is derived from the F-test, measures the probability that the observed difference among group means occurred purely by chance. A low p-value, typically below 0.05, provides strong evidence against the null hypothesis, indicating that at least one predictor has a statistically significant effect on the response variable. Conversely, a high p-value suggests that any observed differences are likely due to random variation.

Pareto charts are often used to display the estimated effects of factors on the response, each bar corresponds to an effect size, sorted in descending order of magnitude, and a reference line that is drawn to mark statistical significance. This chart quickly identifies the most influential terms (those crossing the significance line), indicating the factors or interactions that are most important [43]. Just as the ANOVA table, residual plots are used to diagnose the model adequacy [43], and common residual graphs include:

- Normal probability plot of residuals that checks the normality assumption of errors.
- Residuals versus fitted values, check the constant variance and model form. In a good model the residual vs fitted values shows a random scatter around zero.
- Residuals versus run order, checks independence and if any factors were missed, the plotted graph should show no trend.
- Histogram shows the frequency of the residuals.

Additionally measures such as R^2 and adjusted R^2 help assess the model's goodness of fit by indicating the proportion of the total variance that is explained by the model, the adjusted R^2 adjusts R^2 for the number of predictors in the model, penalizing if insignificant variables are added to the model. The predicted R^2 is a metric of a model's predictive power on new data, uses the Prediction Residual Sum of Squares to statistically predict responses for new experimental points [41], [42], [43].

Table 3.2 - ANOVA Table (adapted from [42])

Source of variation	Sum of squares	Degrees of Freedom	Mean Squares	F- Value
Regression	SSR	$n\beta - 1$	MSR	MSR/MSE
Error	SSE	$N - n\beta$	MSE	
Total	SST	$N - 1$		

After the statistical model is completed, verification tests are performed to make a final analysis of the goodness of fit and the model predictive power [42].

These steps together provide a rigorous framework for determining whether the factors under study have a genuine impact on the outcome.

3.3 Deposition Process Optimization

Maraging steels are sensitive to processing conditions, so optimization has taken into account to achieve defect free parts, reliable mechanical properties, while ensuring dimensional accuracy and process stability.

For the development of this work the DED-Arc machine developed by DEMI was used, see Figure 3.3 . This machine consists of a 3 axis CNC machine with a working volume of 2.10 x 1.50 x 1.25 m where a *Promig NG 450W torch* is attached. The welding system works with an *OERLIKON* power source, model *CITOWAVE III 520* and an *OERLIKON* control unit, model *DMU W500*. The experiments were conducted in manual mode, both Wire Feed Speed (WFS) and Voltage were manually defined, while the current fluctuated according to the transfer characteristics.

Figure 3.3 - DED-Arc machine

The wire manufacturer recommended M12, M13, M20 or M21 Shielding gas, according to the EN ISO 14175 [35]. Considering this information a M20 welding gas, *Arcal Speed* with composition of 92% Ar + 8% CO_2 and flow rate of 13 L/min was used.

In the conditions applied throughout this work, the transfer process was predominantly characterized by short-circuiting, a mode that generally occurs at relatively low voltage and current ranges, with the waveform analysis confirmed the predominance of this mode. This mechanism can be described in two main phases: the arcing period, during which a droplet forms at the wire tip, and the short-circuit period, when the droplet is transferred to the base metal upon contact. These cycles give rise to synchronized fluctuations in voltage and current, as illustrated in Figure 3.4. It should be noted, however, that depending on the specific combinations of process parameters (e.g., current, voltage, and wire feed speed), other transfer modes may also have taken place [16]. Nevertheless, short-circuit transfer was the most frequently observed and therefore served as the basis for the considerations developed in this work

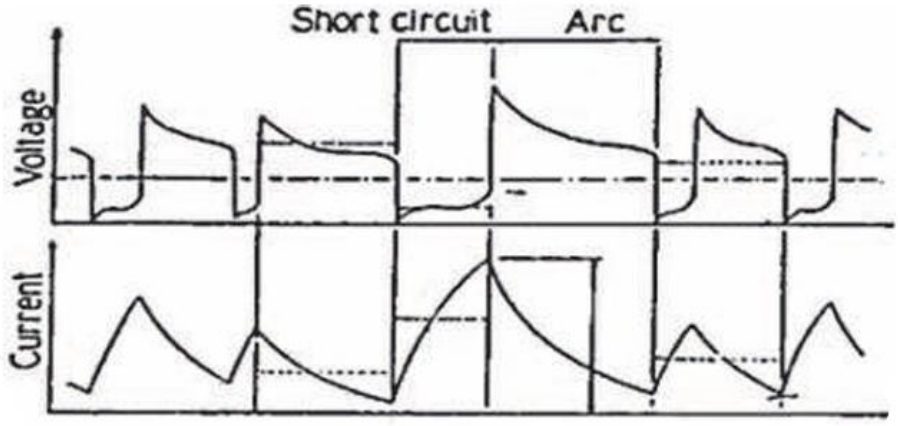

Figure 3.4 - Short Circuit waveforms [16]

The heat input during the metal transfer can be calculated using the equation 3.13, where U is the voltage (V), I the current (A), TS the travel speed (mm/min) and η the efficiency of the GMAW welding process, that was considered 0.8 [4].

$$\boldsymbol{HI} = \frac{\boldsymbol{U} \times \boldsymbol{I}}{\boldsymbol{TS}} \times \boldsymbol{\eta} \left(\frac{\boldsymbol{J}}{\boldsymbol{mm}}\right) \quad 3.13$$

Before performing the Design of Experiments, preliminary tests were carried out, the tests used mild steel substrates with 200 x 60 x 8 mm, every substrate had the same dimensions, to avoid different heat dissipation conditions. Beyond that, substrates with and without a clean surface were used to test the influence of impurities on the material deposition.

Firstly, using wire ER80S-G single bead samples with two layers were made, the lengths of the walls were fixed at 80 mm, a standoff distance of 14 mm and wide parameters of WFS, TS and voltage. Considering the samples made with these parameters and the bibliographic research done, the range of parameters to be used in the DoE were obtained. The parameters are in the Table 3.3.

Table 3.3 - Range of parameters used on the DoE

WFS	TS	Voltage
2,5 - 5,0 m/min	240 - 420 mm/min	18 - 22 V

Secondly, using the parameters from the previous table, samples were made with the material in study (UTP A 702) using the same wall length, shielding gas, substrate dimensions and standoff distance as the previous test. Preliminary visual inspection of the weld beads showed surface discoloration typical of oxidation at welding temperatures (~1400 °C). However, this does not necessarily indicate that maraging steel is especially prone to oxidation, as such reactions occur in most alloys under similar thermal conditions. In maraging steels, surface oxides mainly consist of Fe- and Ni-rich compounds, and their presence alone does not imply reduced weld quality or corrosion resistance [44]. Nevertheless, to reduce the extent of surface oxidation and minimize potential contamination from the substrate, the experimental procedure was adjusted: prior to material deposition, the substrates were sanded to remove surface impurities, and the shielding gas was changed to pure argon with a flow rate of 18 L/min to improve protection of the molten pool.

With the goal of optimizing the parameters of deposition a Design of Experiments was carried out using the methodology of the chapter 3.2 and the statistical software *Minitab*. The DoE planning consists of three factors, Wire Feed Speed (WFS), Travel Speed (TS) and Voltage, these parameters were selected because they are the main factors governing the balance between heat input, deposition rate and arc stability. Among the possible output variables, arc stability was selected as the primary response variable, due to its critical role in ensuring consistent metal transfer and overall process reliability. Each parameter has five factor, to properly model quadratic relationships, this way using the statistical model from the DoE we obtain the values of the parameters that allow us to obtain the higher arc stability. With the goal of increasing precision and estimating experimental error three replicates are used. This way, per replicate, the design planning has eight cube vertices, six star points and six central points, with 20 unique experiments required, equaling in total 60 experiments.

The experiments were randomized, on *Minitab,* to prevent systematic errors and time-based biases, ensuring statistical validity. In this manner, the 60 runs were carried out as presented on Table 3.4. The square brackets represent the coded units.

Table 3.4 - Experimental Planning parameters

Run	TS	WFS	V
1	240 [-1]	5 [1]	18 [-1]
2	330 [0]	3,8 [0.04]	20 [0]
3	420 [1]	2,5 [-1]	18 [-1]
4	240 [-1]	2,5 [-1]	18 [-1]
5	330 [0]	5,9 [1.72]	20 [0]
6	420 [1]	5 [1]	22 [1]
7	330 [0]	3,8 [0.04]	20 [0]
8	178,6 [-1.68222]	3,8 [0.04]	20 [0]
9	481,4 [1.68222]	3,8 [0.04]	20 [0]
10	330 [0]	3,8 [0.04]	16,6 [-1.7]
11	420 [1]	5 [1]	18 [-1]
12	330 [0]	3,8 [0.04]	23,4 [1.7]
13	330 [0]	3,8 [0.04]	20 [0]
14	330 [0]	3,8 [0.04]	20 [0]
15	420 [1]	2,5 [-1]	22 [1]
16	240 [-1]	2,5 [-1]	22 [1]
17	240 [-1]	5 [1]	22 [1]
18	330 [0]	3,8 [0.04]	20 [0]
19	330 [0]	1,6 [-1.72]	20 [0]
20	330 [0]	3,8 [0.04]	20 [0]
21	420 [1]	5 [1]	18 [-1]
22	240 [-1]	5 [1]	22 [1]
23	330 [0]	3,8 [0.04]	20 [0]
24	178,6 [-1.68222]	3,8 [0.04]	20 [0]
25	481,4 [1.68222]	3,8 [0.04]	20 [0]
26	330 [0]	3,8 [0.04]	20 [0]
27	330 [0]	3,8 [0.04]	20 [0]
28	240 [-1]	2,5 [-1]	22 [1]
29	330 [0]	3,8 [0.04]	20 [0]
30	330 [0]	3,8 [0.04]	20 [0]

Run	TS	WFS	V
31	240 [-1]	5 [1]	18 [-1]
32	420 [1]	2,5 [-1]	18 [-1]
33	330 [0]	1,6 [-1.72]	20 [0]
34	420 [1]	5 [1]	22 [1]
35	330 [0]	5,9 [1.72]	20 [0]
36	330 [0]	3,8 [0.04]	23,4 [1.7]
37	420 [1]	2,5 [-1]	22 [1]
38	330 [0]	3,8 [0.04]	16,6 [-1.7]
39	240 [-1]	2,5 [-1]	18 [-1]
40	330 [0]	3,8 [0.04]	20 [0]
41	330 [0]	5,9 [1.72]	20 [0]
42	420 [1]	5 [1]	18 [-1]
43	330 [0]	3,8 [0.04]	20 [0]
44	420 [1]	2,5 [-1]	18 [-1]
45	420 [1]	2,5 [-1]	22 [1]
46	178,6 [-1.68222]	3,8 [0.04]	20 [0]
47	240 [-1]	5 [1]	18 [-1]
48	330 [0]	3,8 [0.04]	23,4 [1.7]
49	330 [0]	1,6 [-1.72]	20 [0]
50	330 [0]	3,8 [0.04]	20 [0]
51	330 [0]	3,8 [0.04]	20 [0]
52	330 [0]	3,8 [0.04]	16,6 [-1.7]
53	420 [1]	5 [1]	22 [1]
54	330 [0]	3,8 [0.04]	20 [0]
55	240 [-1]	5 [1]	22 [1]
56	240 [-1]	2,5 [-1]	22 [1]
57	330 [0]	3,8 [0.04]	20 [0]
58	481,4 [1.68222]	3,8 [0.04]	20 [0]
59	240 [-1]	2,5 [-1]	18 [-1]
60	330 [0]	3,8 [0.04]	20 [0]

The arc stability was measured in a similar manner to the study made by A. Rocha [28]. The voltage and current acquisition system consisted of a Hall effect probe, a voltage divider and a signal acquisition board, brand *DIGILENT* model *Analog Discovery 2.* The Hall probe detects the magnetic field generated by the current flowing through the cable, the voltage divider, connected in parallel, works with a positive crocodile connected to the torch and a negative crocodile to the weld table, using resistors to scale down high voltage to a lower one. The *DIGILENT* acquires the input signals, with acquisition rate of 10 kHz, ensuring sufficient resolution to capture short-circuit events and voltage fluctuations (this frequency was chosen based on prior studies and hardware capabilities) that are converted into digital data (waveforms) to be analyzed. The system is calibrated with compensation factors of 149.4586 for current and 30.8745 for voltage.

The arc stability was evaluated based on the period between successive short-circuit cycles identified in the voltage signal of the welding process. The Arc Stability Index (S) was then calculated using Equation 3.14 where the $\bar{T}$ and the S_T are the mean and standard deviation of the short circuit period, respectively. The closer the arc stability index is to 100 % the stabler the electric arc [28]. The code developed in Python, is provided in Appendix A.

$$\boldsymbol{S = 100 \times (1 - \frac{S_T}{\bar{T}})} \quad (\%) \qquad \mathbf{3.14}$$

The code takes a text file as input, containing time data for voltage and current measured during the welding experiments, reading it skipping comments or headers and scaling the signals based on the calibration constants. Using the voltage signal, it detects the start of the arc by finding the first voltage value that exceeds the defined threshold, the time axis is shifted to this arc start with $t = 0$. To reduce interference from noise, the input signals are passed through a 50 Hz notch filter, and the waveforms are plotted with all significant voltage dips, these relevant dips occur when the voltage drops below a specified threshold and are spaced apart by minimum time interval to avoid detecting multiple hits on one dip. With the goal of obtaining precise measurements of arc stability between different processes, the code selects the first 30 dips after 2.5 s from the start of the arc and calculates the time intervals between them.

The outputs are arc stability index, mean period, standard deviation of dip intervals and a waveform showing the dips used on the Arc Stability Index calculation, as observed on Figure 3.5.

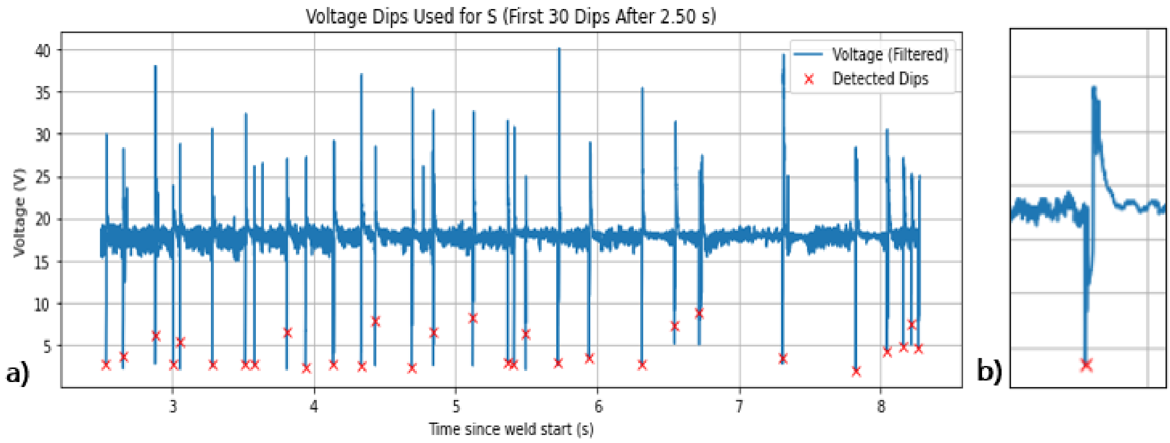

Figure 3.5 - Voltage Waveform: a) Significant Voltage Dips (Run 4), b) voltage dip at instance t= 5.9 s

Due to the results explained in the Chapter 4, the arc stability was evaluated again, but in this case, the analysis was based on the signal amplitude rather than on the period between short circuit cycles. This method to measure the arc stability is grounded and empirically supported by previous works, such as Suban and Tušek [45]. The authors highlight that one of the most effective methods to evaluate a welding process stability is the statistical analysis of voltage and current signals in the time domain. Measuring the fluctuations in these signals is a reliable way to assess consistently the arc behavior, with greater fluctuations (higher standard deviations) interpreted as indicators of instability. The arc stability index (S) is determined from the voltage signal using equation 3.15, where σ_V represents the standard deviation of the voltage and μ_V the mean voltage of the signal. Producing lower stability values for unstable arc and higher values for stable ones.

$$S = 100 \times \left(1 - \frac{\sigma_V}{\mu_V}\right) \quad (\%) \qquad 3.15$$

In their experimental setup, authors emphasize the importance of preprocessing raw data using low pass filters in order to reduce high-frequency noise [45].

The data was analyzed using the code on *Appendix B,* followed by the DOE (equal to the short circuit period-based analysis). After this stage the most appropriate deposition parameters for the established objectives were determined.

3.4 Mechanical and Microstructural Characterization

To assess the mechanical properties and the microstructure of the material deposited using the process parameters determined with the DOE, uniaxial tensile testing and metallographic analysis were performed to confirm if the new deposition parameters achieved the desired mechanical properties, relationship between the microstructure and mechanical properties and evaluate the Heat treatment effects.

The uniaxial tensile tests were conducted on a *StepLAB EA05,* static testing machine, with a load cell that allows a maximum static force of 15.00 kN [46]. The tests were performed at room temperature and with a displacement speed of 0,017 mm/s.

For the uniaxial tensile testing, samples were made following the ISO 6892-1:2019 [47]. The specimen dimensions were adjusted from the standard to align with the capabilities of the available tensile testing equipment and the constraints dictated by the sample size

Following the previously mentioned sample standard, the sample has the dimensions shown in Figure 3.6.

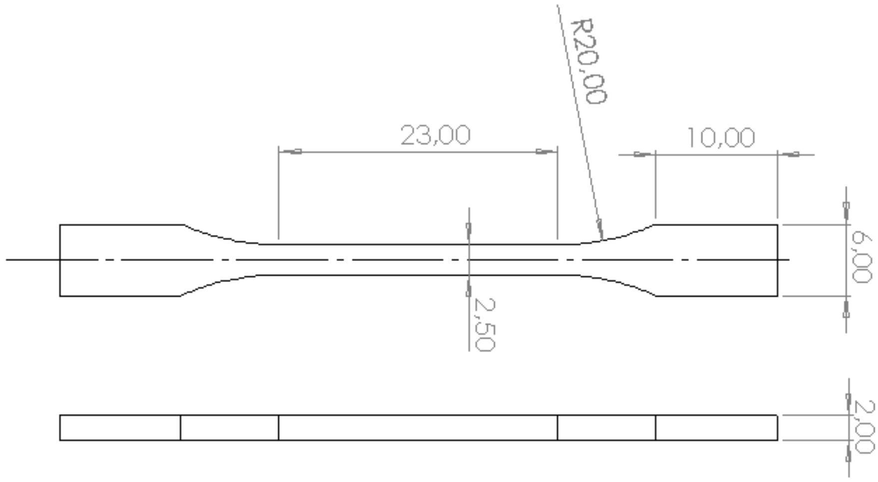

Figure 3.6 - Uniaxial tensile test specimen's dimensions

The tensile test specimens were produced from two walls, made using the same optimized deposition parameters, the use of distinct walls allowed us to evaluate the reproducibility of the process by checking if the samples yield consistent mechanical properties. If variability arises, because we have samples from two builds we can identify whether the variability is random or build-specific. Both walls were made using one welding bead, the first wall was made with a length of 170 mm and 80 mm of height, see Figure 3.7. The second wall was made with a length of 210 mm and 80 mm of height, the reason for a higher length than the second wall was the need to produce more tensile samples.

Figure 3.7 - Wall 1 (Deposited State): a) Front view; b) Top view

After being deposited, the walls were face-milled on a manual milling machine and cut on a band saw to ensure flatness on the wall sides. This process is followed by the rectification of these parts on a conventional flat grinding machine to ensure surface finishing and a uniform specimen thickness of 2.0 mm, the Figure 3.8 shows the parts after this process.

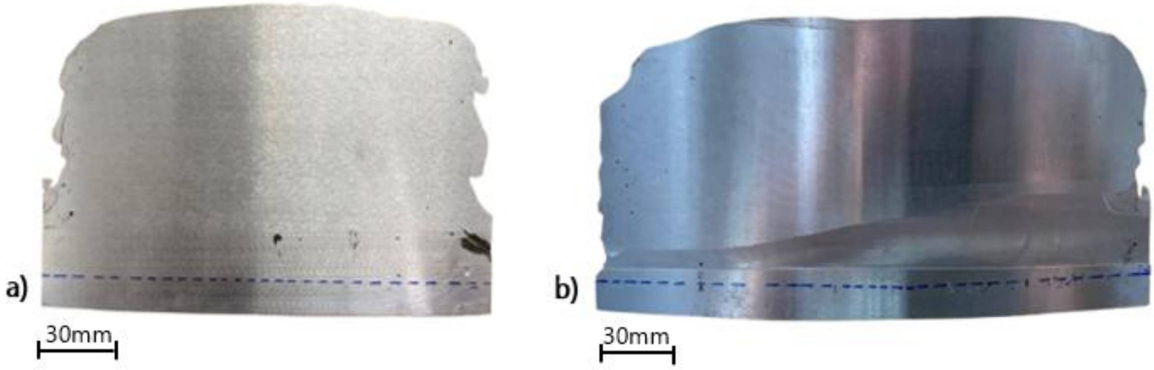

Figure 3.8 - Machined Walls to produce tensile samples, blues line is the border between substrate and deposited material: a) Wall 1; b) Wall 2

The samples were machined from these walls using a *HAAS Super Mini Mill 2* machining center, were machined 19 samples being removed 9 vertical samples (along the build direction) and 10 horizontal samples (along the deposition direction). Extracting both vertical and horizontal samples is important to evaluate if the anisotropic nature of additive manufacturing leads to the mechanical properties being direction dependent due to the layer-by-layer deposition [30]. The machined samples are shown in Figure 3.9. This is followed by cutting the samples from the building wall and sanded.

a)
b)

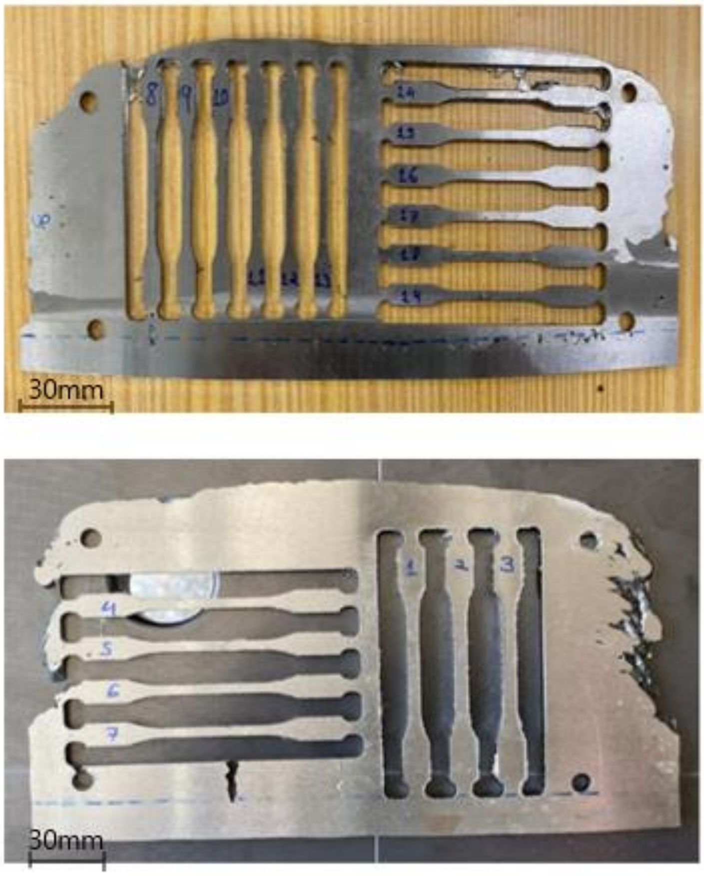

Figure 3.9 - Location and direction of samples on the machined walls: a) Samples Wall 2; b) Samples Wall 1

Then to test the heat treatment, we separated 8 samples (4 vertical and 4 horizontal) to test the influence of the post process treatment. Before realizing the uniaxial tensile testing, the samples were identified, sanded and measured, this information is organized in the Table 3.5.

Table 3.5 - Samples used on the uniaxial tensile test

	Number	Direction	Thickness (mm)	Width (mm)
Without heat treatment	2	Vertical	2,10	2,50
	6	Horizontal	2,08	2,54
	7	Horizontal	2,10	2,50
	10	Vertical	2,14	2,52
	11	Vertical	2,14	2,50
	12	Vertical	2,14	2,48
	13	Vertical	2,14	2,54
	15	Horizontal	2,16	2,56
	17	Horizontal	2,12	2,46
	18	Horizontal	2,06	2,48
	19	Horizontal	1.84	2,52
With heat treatment	1	Vertical	2,10	2,56
	3	Vertical	2,10	2,56
	4	Horizontal	2,08	2,52
	5	Horizontal	2,10	2,50
	8	Vertical	2,20	2,56
	9	Vertical	2,12	2,52
	14	Horizontal	2,30	2,54
	16	Horizontal	2,10	2,54

A *Hitachi SU3800 Scanning Electron Microscope* (SEM) was used to analyze the fracture surfaces of the specimens subjected to uniaxial tensile testing. Gaining insights into the fracture mode, presence of microstructural defects and the correlation between mechanical performance and microstructure.

To study the microstructure of the samples, a new wall was fabricated, and a section was cut from the center of the deposited wall using a band saw. We produced two samples, one with and one without heat treatment, these were embedded in epoxy resin, rectified and polished using sandpaper with gradually finer grain sizes, from P80 to P2500, followed by a BUEHLER diamond paste. To observe the microstructure, the samples were contrasted with an acidic solution, the solution consisted of Nital 3% in volume, 97% Etanol and 3% Nitric Acid, the samples were immersed during 5s.

The microscope *Leica DMI 5000 M* was used to observe the samples. Images were taken in 3 zones of interest, this is the upper, middle and lower location of the samples. This approach ensures a comprehensive understanding of how grain morphology, phase composition and potential defects evolve along the building direction. Different grades of magnification were used to observe the overall build structure and grain morphology.

4 Results and Discussion

4.1 Response Surface Analysis

In the following section, the fitted response surface models are presented and analyzed. This includes model adequacy checking, analysis of variance (ANOVA), significance of regression coefficients, and the generation of response surface and contour plots. Finally, the optimal conditions predicted by the model are discussed.

Firstly, the Model Fit and Significance of the method that uses the short circuit period to measure the arc stability of the deposition process was analyzed, using the ANOVA table (Table 4.1), with SS being the Sum of Squares and MS the Mean Square. The overall Model F-Value of 8.11 ($p<0.0001$) means that the regression model explains a significant portion of the variation in the arc stability, this value lets us reject the null hypothesis that all the factors have zero effect, confirming that the model is statistically significant in establishing a correlation between the input variables and output responses. Therefore, the independent variables (WFS, TS, V) influence the arc stability of the process [41] .

Table 4.1 - ANOVA Table for short circuit period based Arc Stability

Source	*DF*	*SS (Adj.)*	*MS (Adj.)*	*F-Value*	*P-Value*
Model	9	3641.22	404.58	8.11	0.0
Linear	3	876.08	292.03	5.85	0.002
Travel Speed (mm/min)	1	3.7	3.7	0.07	0.786
Wire Feed Speed (m/min)	1	810.4	810.4	16.25	0.0
Voltage (V)	1	62.72	62.72	1.26	0.268
Quadratic	3	2512.44	837.48	16.79	0.0
Travel Speed^2	1	1.38	1.38	0.03	0.869
Wire Feed Speed^2	1	2453.57	2453.57	49.19	0.0
Voltage^2	1	76.88	76.88	1.54	0.22

Two-Factor Interaction	3	198.08	66.03	1.32	0.277
Travel Speed × Wire Feed Speed	1	21.49	21.49	0.43	0.515
Travel Speed × Voltage	1	173.83	173.83	3.49	0.068
Wire Feed Speed × Voltage	1	2.76	2.76	0.06	0.815
Error	50	2493.9	49.88		
Lack of Fit	6	986.4	164.4	4.8	0.001
Pure Error	44	1507.5	34.26		
Total	59	6135.12			

Having a statistically significant model the next step is to analyse the goodness of fit. The lack of fit is significant (F=4.80) with the probability of this magnitude arising from random variation is 0.1%, meaning that the residual error (discrepancy between observed and predicted values) is larger than would be expected from pure experimental noise and that the quadratic model does not capture all the structure data [41].

The model summary (Table 4.2) , shows this lack of fit. Resulting in a high residual error of 7.06242, the actual values deviate from the predicted values by ±7.06 units of the response variable, and low prediction capability with predicted R^2 only 38.65%, thus the model isn't fitted enough to optimize the deposition process.

Table 4.2 - Model Summary table for short circuit period-based Arc Stability

S	*R2*	*R2(aj)*	*R2(pred)*
7.06243	59.35%	52,03%	38,65%

The short-circuit period method did not provide reliable results for UTP A 702. The events occurred in a discrete and unpredictable behavior, producing significant scatter and non-linearity in the data, which led to the lack of fit observed in the ANOVA analysis. This behavior is linked to the distinctive thermal and physical characteristics of maraging steels and the stochastic behavior of short-circuits during droplet detachment that causes abrupt voltage and current fluctuations. Its high sensitivity to heat input, uneven thermal gradients along the deposition path, and heat buildup in the contact tip of the torch alter wire melting behavior and destabilize the arc. As a result, short-circuit patterns varied irregularly between runs, reducing measurement consistency and limiting the suitability of this method for DOE optimization.

These behaviors could potentially be accounted for in the model if additional variables, such as heat accumulation in the contact tip or variations in surface tension were measured and included as independent factors in the Design of Experiments [48].

The arc voltage was chosen to measure the arc stability; it is a continuous signal that accurately reflects the dynamic behavior of the arc, including arc length, plasma conditions, and transfer mode. The mean voltage gives a simple baseline of the arc's operating level, while the standard deviation measures how much the voltage departs from that baseline, dips caused by short circuits. These two easy to compute statistics together capture both the typical arc condition and its variability, making them practical inputs for a normalized stability metric and suitable response variables for response surface methodology [45].

The DOE was performed for this method, with the following ANOVA Table presented in Table 4.3. The overall model has F=28.18 ($p<0.001$), confirming that the model is highly significant and a large fraction of the arc stability behavior can be explained by the model. Regarding the model fit, the lack-of-fit test has F=0.80 with p=0.577 indicating that the model doesn't show a significant lack of fit due to pure error. The model summary (Table 4.4), gives us that the 83% of the variability in arc stability is explained by the model, the model is not overfitted with adjusted R^2 80.57% and is robust enough to predict the arc stability for new parameter settings.

Overall ANOVA suggests a good model, that is statistically significant and has a low lack of fit.

Table 4.3 - ANOVA Table for voltage based Arc Stability

Source	*DF*	*SS (Adj.)*	*MS (Adj.)*	*F-Value*	*P-Value*
Model	9	411.355	45.706	28.18	0.0
Linear	3	356.888	188.963	73.34	0.0
Travel Speed (mm/min)	1	5.118	5.118	3.16	0.082
Wire Feed Speed (m/min)	1	148.367	148.367	91.47	0.0
Voltage (V)	1	202.833	202.833	125.04	0.0
Quadratic	3	9.271	3.090	1.91	0.141
Travel Speed^2	1	3.112	3.112	1.92	0.172
Wire Feed Speed^2	1	5.152	5.152	3.18	0.081
Voltage^2	1	0.004	0.004	0.00	0.963

Two-Factor Interaction	3	40.815	13.605	8.39	0.0
Travel Speed × Wire Feed Speed	1	5.413	5.413	3.34	0.074
Travel Speed × Voltage	1	0.191	0.191	0.12	0.733
Wire Feed Speed × Voltage	1	35.212	35.212	21.71	0.0
Error	50	81.105	1.622		
Lack of Fit	6	7.957	1.326	0.80	0.577
Pure Error	44	73.148	1.662		
Total	59	492.460			

Table 4.4 - Model Summary table for voltage based Arc Stability

S	*R2*	*R2(aj)*	*R2(pred)*
1.27362	83.53%	80.57%	75.60%

The ANOVA results support the model's structure by identifying which factors meaningfully influence arc stability. Wire feed speed, voltage, and their interaction stand out as the most statistically significant, while all other terms, like travel speed, quadratic effects, and the remaining interactions, do not meet the significance threshold. This indicates that, within the experimental range, arc stability responds primarily to linear changes in WFS and voltage, and that these two variables must be adjusted in tandem to achieve optimal performance.

The lack of statistical significance for travel speed suggests that its influence on arc behavior is minimal. Likewise, the non-significance of the quadratic terms implies a predominantly linear relationship between the inputs and the response, with no strong evidence of curvature in the response surface.

As a result, the model could be reduced to include only significant terms, while retaining the model’s predictive power. In practical terms, this means that process optimization efforts for arc stability in DED-Arc should focus on the coordinated control of wire feed speed and voltage, as illustrated by the Pareto chart in Figure 4.1.

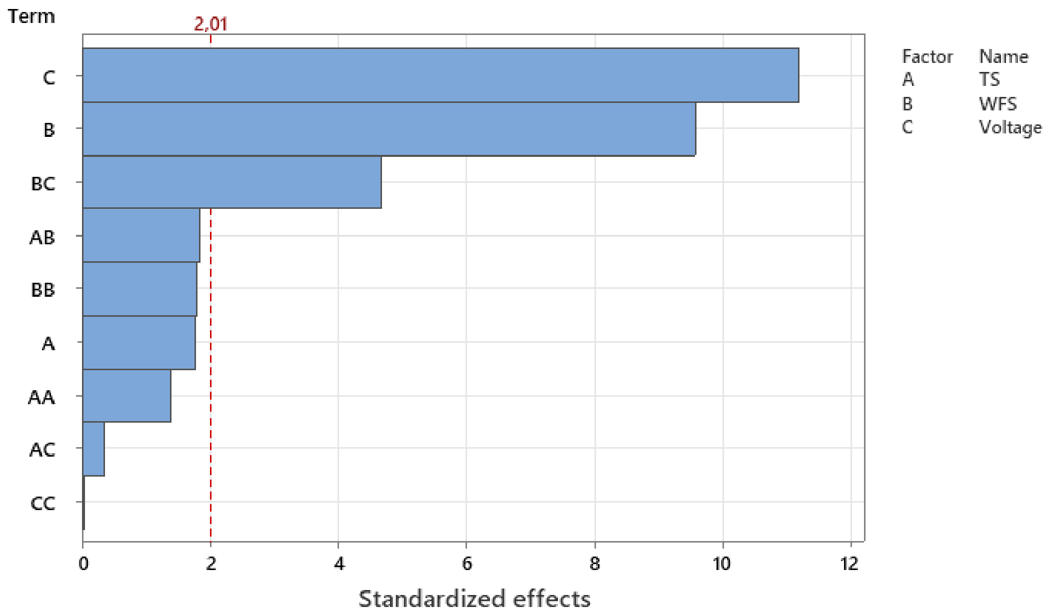

Figure 4.1 - Pareto chart of Standardized effects

The residual analysis shown in Figure 4.2, supports the adequacy of the regression model used to describe the arc stability. The normal probability plot of the residuals falls approximately along a straight line, the plotted residuals closely follow the reference line, with no systematic curvature or substantial deviations. This strongly indicates that the normality assumption is satisfied, which validates the use of parametric inference methods such as p-values and confidence intervals. Complementing this, the histogram of residuals is relatively symmetric and centered around zero, forming a bell-shaped pattern characteristic of a normal distribution, reinforcing the conclusion that the residuals can be considered approximately normal. For the plot of residuals versus fitted values, although the overall distribution of residuals is relatively balanced around the zero line, there are slight clusters of residuals at specific ranges of fitted values. These clusters may suggest mild heteroscedasticity or local patterns not fully captured by the model. However, the clustering is not severe and does not display any systematic trend such as funnel shapes or curvature, which would indicate more serious violations. As such, the assumption of constant variance is mostly acceptable. Finally, the residuals versus observation order plot are randomly distributed over the run order, without visible trends or cycles. This indicates that the residuals are independent and unaffected by the experimental sequence [43].

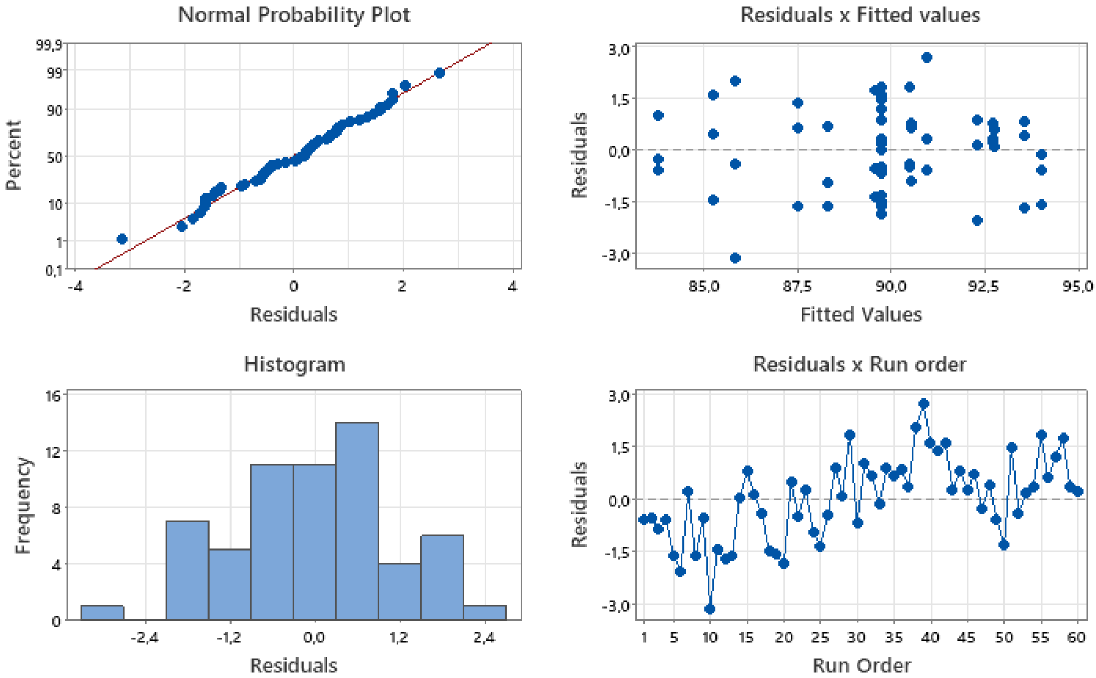

Figure 4.2 - Residual Plots for Arc Stability

All four diagnostic plots support the validity of the regression model. The residuals are approximately normally distributed, exhibit constant variance, are independent, and show no signs of model misspecification.

To evaluate the effects of the process parameters, surface plots illustrated in Figure 4.3 are generated through Response Surface Methodology (RSM), illustrating the interaction between two parameters simultaneously while holding constant the third constant (TS = 330 mm/min, WFS = 3.75 m/min, Voltage = 20 V).

In the plot of TS versus WFS (Figure 4.3.a), arc stability displays a nonlinear trend, with a noticeable curvature indicating interaction between the two parameters. Stability tends to improve at moderate values of both TS and WFS, suggesting the existence of an optimal combination that balances deposition rate and arc behavior.

The plot of TS versus voltage (Figure 4.3.b) reveals that arc stability generally increases with higher voltage. This trend is explained by the phenomenology of arc behavior: higher voltage increases arc length and reduces short-circuit frequency. A longer arc promotes uniform heat input, smoother droplet detachment, and consistent energy transfer to the weld pool, which collectively reduces fluctuations and enhances arc stability.

Finally, the WFS versus voltage plot (Figure 4.3.c) demonstrates a strong positive correlation between both parameters and arc stability. Higher values of WFS and voltage result in significantly improved arc behavior. This is likely due to enhanced metal transfer modes and reduced arc wandering, due to the increase in arc length when the arc is sufficiently powered, and consistent material feed.

These plots collectively highlight the importance of parameter interactions in influencing arc stability, the trends observed support the need for a multivariable optimization strategy. The contour plots can be observed in Appendix C.

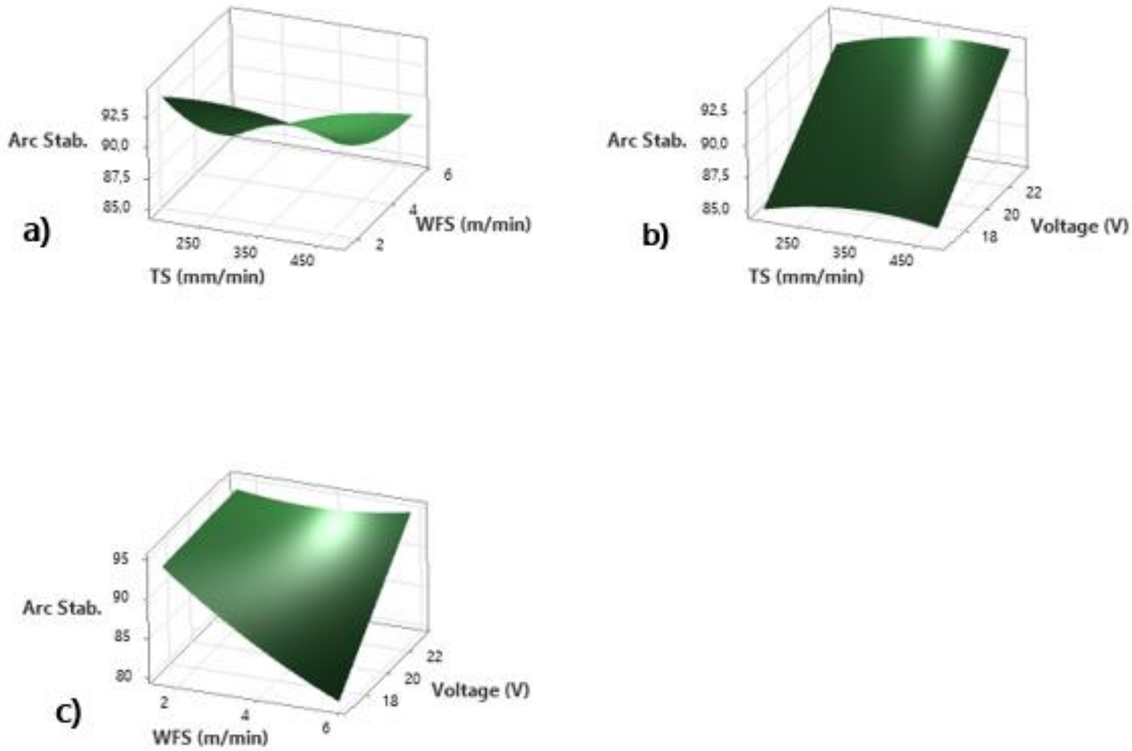

Figure 4.3 - Surface Plots of Arc Stability with process variables: a) Effect of TS and WFS on Arc Stability, b) Effect of TS and Voltage on Arc Stability, c) Effect of WFS and Voltage on Arc Stability

The optimization phase was carried out using the Response Optimizer tool in *Minitab.* It uses a numerical optimization algorithm that evaluates the fitted model equation, in this case searched for parameter values that would maximize the response, arc stability. Equation 4.1 shows the fitted model equation, following the general second order polynomial (equation 3.6), enabling the identification of both individual and combined effects.

$$\boldsymbol{Arc\ Stability} = \mathbf{115.3 + 0.0001 \cdot \boldsymbol{TS} - 14.19 \cdot \boldsymbol{WFS} - 0.78 \cdot \boldsymbol{V} - 0.0000332 \cdot \boldsymbol{TS2} + 0.213 \cdot \boldsymbol{WFS2} - 0.0022 \cdot \boldsymbol{V2} + 0.00422 \cdot \boldsymbol{TS} \cdot \boldsymbol{WFS} + 0.00050 \cdot \boldsymbol{TS} \cdot \boldsymbol{V} + 0.484 \cdot \boldsymbol{WFS} \cdot \boldsymbol{V}} \tag{4.1}$$

The optimization identified the ideal parameter configuration as indicated on Table 4.5, with a composite desirability score of 1.000 that confirms that the optimization precisely met the defined objective of maximizing arc stability. The model predicted an arc stability value of 96.28, with a 95% confidence interval ranging from 92.99 to 99.58. The 95% prediction interval, accounting for variation in future runs, extends from 92.11 to 100.46.

Table 4.5 - Optimized Deposition Variables

TS	WFS	Voltage
481.4 mm/min	5.9 mm/min	23.4 V

In practical terms, within the studied variable domain, the optimized settings provide a reliable starting point, with joint control of wire feed speed and voltage essential for maximizing arc stability while travel speed may be treated as a secondary factor.

4.2 Uniaxial Tensile Testing

Additively manufactured components often exhibit anisotropic properties, meaning their mechanical behavior differs between the vertical and horizontal directions. This anisotropy is largely driven by the heterogeneous microstructure along the height of the wall. In most cases, vertical specimens show lower mechanical strength than horizontal specimens, as their loading axis is perpendicular to the deposition direction, resulting in a greater number of interlayer boundaries within the gauge length [29], [30]. But studies conducted with maraging steel 18Ni-350 [23], [27], showed that the vertical values of UTS, YS and elongation are higher than the horizontal values.

Ultimate tensile strength (UTS) and elongation to fracture were measured and the results presented in Table 4.6, this table includes only the valid results obtained from the uniaxial tensile tests to see the remaining the Appendix E can be consulted. The fractured samples can be observed on Appendix D.

Table 4.6 - Results from the uniaxial tensile tests performed in samples made by DED-Arc

Direction	Sample number	UTS (MPa)		Elongation (%)		Heat treatment
Vertical	10	1230	1366	5.8	6.6	Without
	11	1380		7.3		
	13	1490		6.8		
	1	1650	1613	8.0	8.5	Aging
	3	1650		8.4		
	8	1540		9.0		
Horizontal	19	1190	1253	5.6	5.9	Without
	7	1290		5.7		
	15	1280		6.3		
	5	1700	1686	12	10.2	Aging
	14	1650		12		
	16	1710		6.5		

The fracture at the gauge marks was likely caused by the overtightening of the mechanical grips to prevent slippage during loading. Excessive clamping force can create stress concentrations that promote premature fracture near the gauge mark, this can be exacerbated by slight misalignment during gripping. A suitable solution includes the use of hydraulic grips that allows uniform clamping pressure through the test without inducing localized stress and increasing the gauge-shoulder transition radius to reduce geometric stress concentrations.

We had outlier results in samples 17 and 18, whose UTS and elongation values deviated from the dataset mean. The most probable cause is localized microstructural defects associated with the DED-Arc process, such as inclusions or lack of fusion, likely resulting from fluctuations in wire positioning or brief process interruptions during deposition.

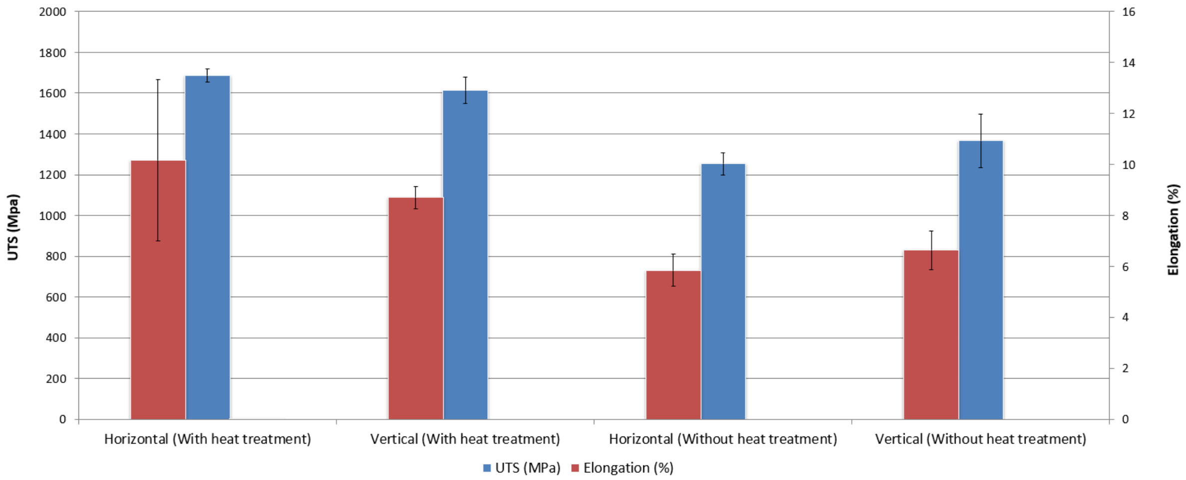

Figure 4.4 - Overview of mechanical properties of samples with standard deviation

In the as build condition, the ultimate tensile strength (UTS) ranged between 1253 MPa (Horizontal build) and 1366 MPa (Vertical build). Elongation to fracture, under these conditions, varied between 5.85% in the horizontal direction and 6.6% in the vertical direction. Following the prescribed aging heat treatment, all mechanical properties showed a notable increase. The UTS rose to 1686,7 MPa (Horizontal) and 1613,3 MPa (Vertical), elongation values also improved, reaching 10.17% for the horizontal build direction and 8.5 % for the vertical build direction. These values are organized in Figure 4.4.

The mechanical properties, in the as build state are according to the literature, these properties are explained by the direction of dendrite and intergranular structure in the vertical direction, with loading forces parallel to this direction being resisted by both dendrite and intergranular structure, in perpendicular loads the inter granular region acts as a weakened region and fractures prematurely [23], [27].

The increase in UTS and elongation is attributed to the tempering of the martensitic matrix and the precipitation of nanoscale intermetallic phases, which relives internal stresses while providing additional precipitation strengthening.

After aging, the horizontal samples exhibited higher elongation than the vertical ones, showing that columnar grain structures and interlayer interfaces produce pronounced build direction anisotropy. Aging induced a fine dispersion of Ni–Ti and Mo rich intermetallic precipitates that increased strength by precipitation hardening while creating localized nanoscale heterogeneities, consequently, vertical oriented samples, whose loading axis intersects elongated grains and numerous layer boundaries, are more susceptible to loss of ductility. Niu et al. [49] directly demonstrated rapid Ni–Ti co-clustering and the subsequent formation of Ni_3Ti accompanied by Mo rich nanoparticles during aging raised UTS in all orientations while producing local brittle sites that triggered early crack initiation and lower elongation in mechanically critical orientations. Applying a prior solution treatment would reduce columnar heterogeneity and layer related defects, thereby diminishing the difference between vertical and horizontal specimens.

Representative stress-strain curves for specimens in both transverse and longitudinal orientation, in the as build condition and heat treated, are shown on Figure 4.5.

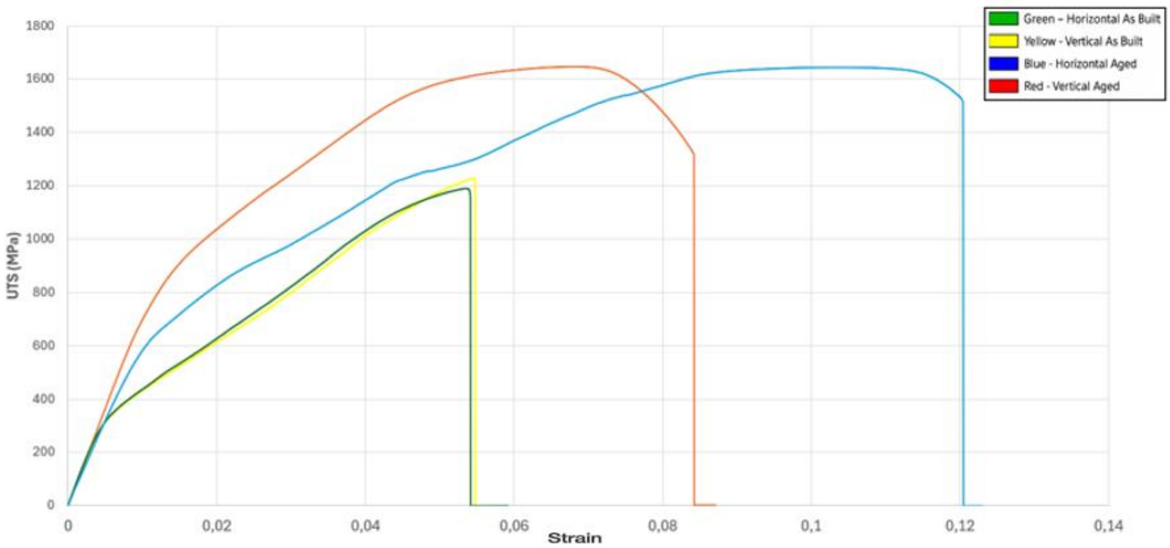

Figure 4.5 - Uniaxial tensile stress-strain curve for the UTP A 702 WAAM Samples in horizontal and vertical orientation, as built and aged condition.

4.3 Microscopic characterization

The performance of DED-Arc maraging steels is greatly determined by their microstructure. As discussed in the literature review, the combined effects of rapid solidification, thermal cycling, and subsequent aging processes leads to the evolution of features such as martensitic laths, reverted austenite, and nanoscale precipitates, which in turn controls the balance of strength and toughness.

The Figure 4.6 shows the microstructure of DED-Arc produced parts at different locations along the built direction. In the bottom region of the deposited wall, the microstructure consists of coarser columnar grains, aligned predominantly with the build direction. Within these grains, the matrix is composed of lath martensite, interspersed with noticeable pools of reverted or retained austenite between grain boundaries and inter-dendritic areas. The middle region has columnar grains, but the grains appear finer and more elongated, still oriented along the built direction. The microstructure is again dominated by martensite, with reverted austenite pockets at inter dendritic areas, but with finer grains reflecting the lower thermal cycles that occurred in comparison to the bottom zone. The top region presents a markedly different morphology. Here, the microstructure is composed of, less columnar, fine dendritic grains. The matrix is almost entirely lath martensite, with only a very small fraction of retained austenite visible and shows less contrast after etching. Compared to the lower regions, the microstructure is significantly more uniform and has smaller feature sizes [26], [33], [50].

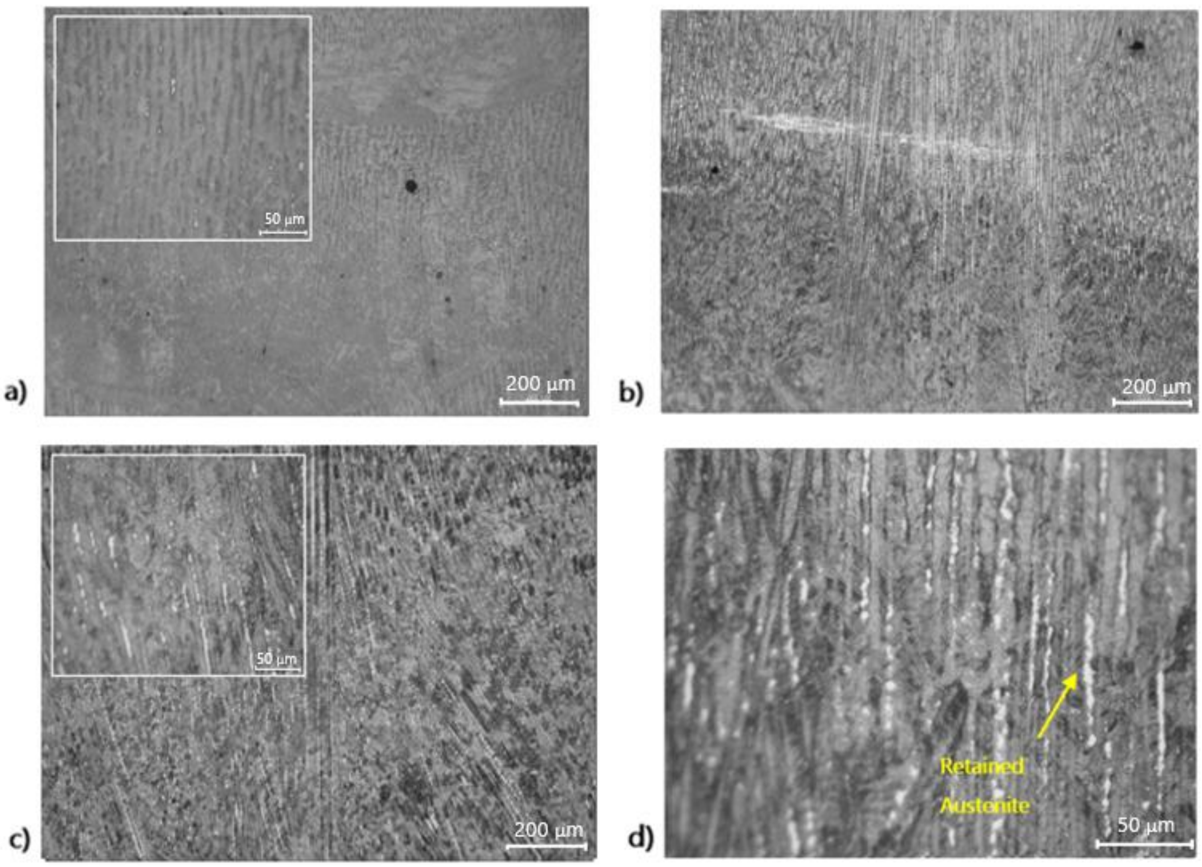

Figure 4.6 - Microstructure of as built samples: a) Top at 200 μm and 50 μm, b) Middle at 200 μm, c) Bottom at 200 μm and 50 μm, d) higher magnification (50 μm) microstructure at the middle.

These variations arise from the thermal history related to the DED-Arc process. At the bottom, the repeated reheating from subsequent passes promotes epitaxial grain growth, causing coarse columnar grains to extend upward through multiple layers. The thermal cycling also enriches inter-dendritic regions in nickel, stabilizing austenite at high temperature and allowing partial reversion upon cooling. Together, these effects are accountable for coarse scale and larger fractions of reverted austenite at the base. In the middle section, the grains still grow epitaxially, but the reheating intensity is reduced compared to the bottom. As a result, grains remain elongated but at smaller dimensions. The presence of austenite pockets continues, though to a lesser degree than in the bottom region [33], [50].

At the top, despite the general trend of slower cooling with increasing part height, the absence of reheating from subsequent layers allows the last deposited material to cool continuously without remelting. This rapid, uninterrupted solidification promotes the formation of finer dendritic structures compared to the reheated lower regions. The lack of prolonged reheating or significant solute redistribution limits the stabilization of reverted austenite, explaining why this region contains the lowest fraction of austenite and the most homogenous martensitic structure [26].

Analyzing the microstructure after aging treatment, see Figure 4.7, the martensitic matrix is strengthened by the precipitation of nanoscale intermetallic precipitates (non-visible), while reverted austenite nucleates at lath and grain boundaries, visible in detail in Figure 4.7d), especially in the lower and middle regions where thermal cycling was more intense. Compared to the as-built state, the martensite laths appear coarser, along with fractions of reverted austenite that increased after aging. Overall, the aged condition microstructure consists of a martensitic matrix with reverted austenite and strengthening precipitates (not visible), the presence of precipitates is still related to the DED-Arc process [26], [27], [33].

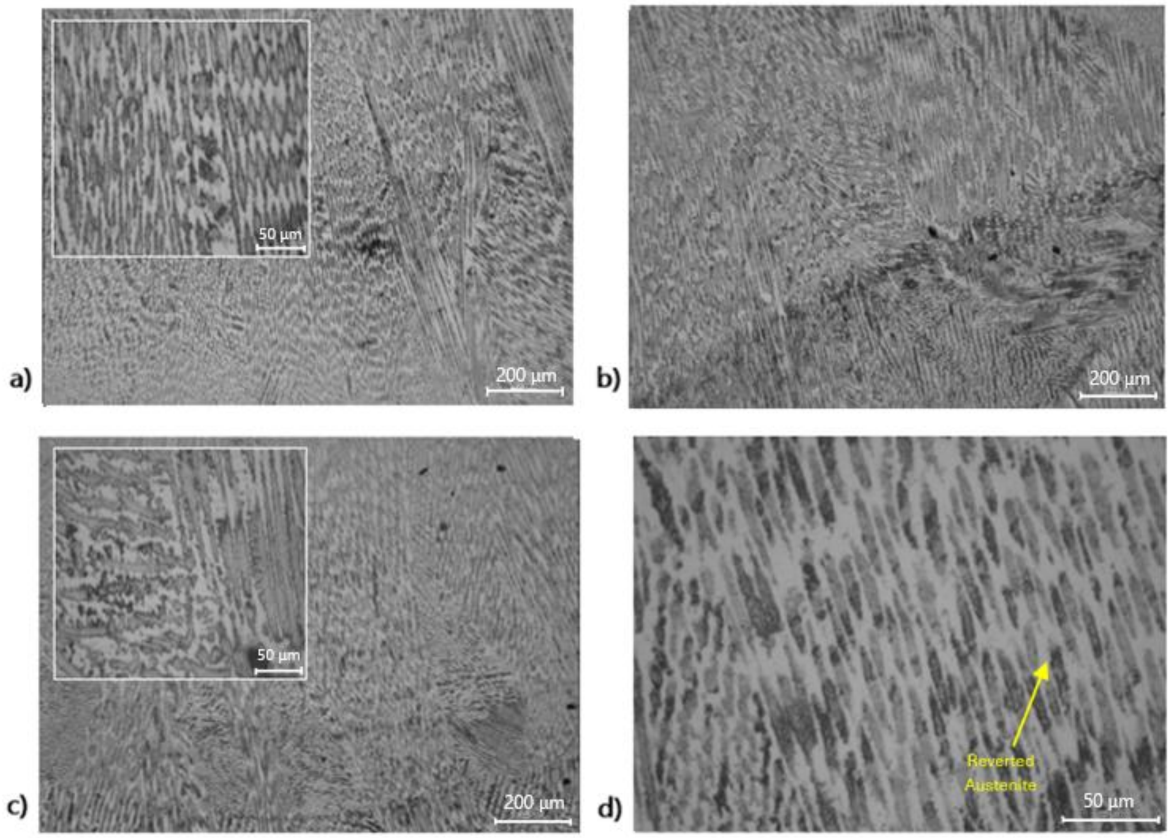

Figure 4.7 - Microstructure of aged samples: a) Top at 200 µm and 50 µm, b) Middle at 200 µm, c) Bottom at 200 µm and 50 µm, d) higher magnification (50 µm) microstructure at the middle.

From the microstructure of aged samples, we can conclude that aging heat treatment slightly reached the over-aged condition. During direct aging, the martensitic matrix underwent tempering, characterized by stress relief and diffusion of alloying elements that promote the formation and coarsening of intermetallic precipitates. As result, the shape of the cellular grains became more regular and the thickness of cellular boundaries widened. A slight increase in average grain size was also observed, associated with the limited growth of martensitic laths during diffusion and the increased presence of reverted austenite. This over-aging leads to a reduction in strength and hardness but an increase in elongation, toughness, and impact energy when compared with normally aged samples. To mitigate over-aging, the duration or temperature of the aging treatment should be reduced [33], [37], [51].

4.4 Fractography

The fracture surfaces of samples submitted to the uniaxial tensile test were inspected using a Scanning Electron Microscope (SEM), as observed on Figure 4.8. To observe the remaining samples, see the Appendix E.

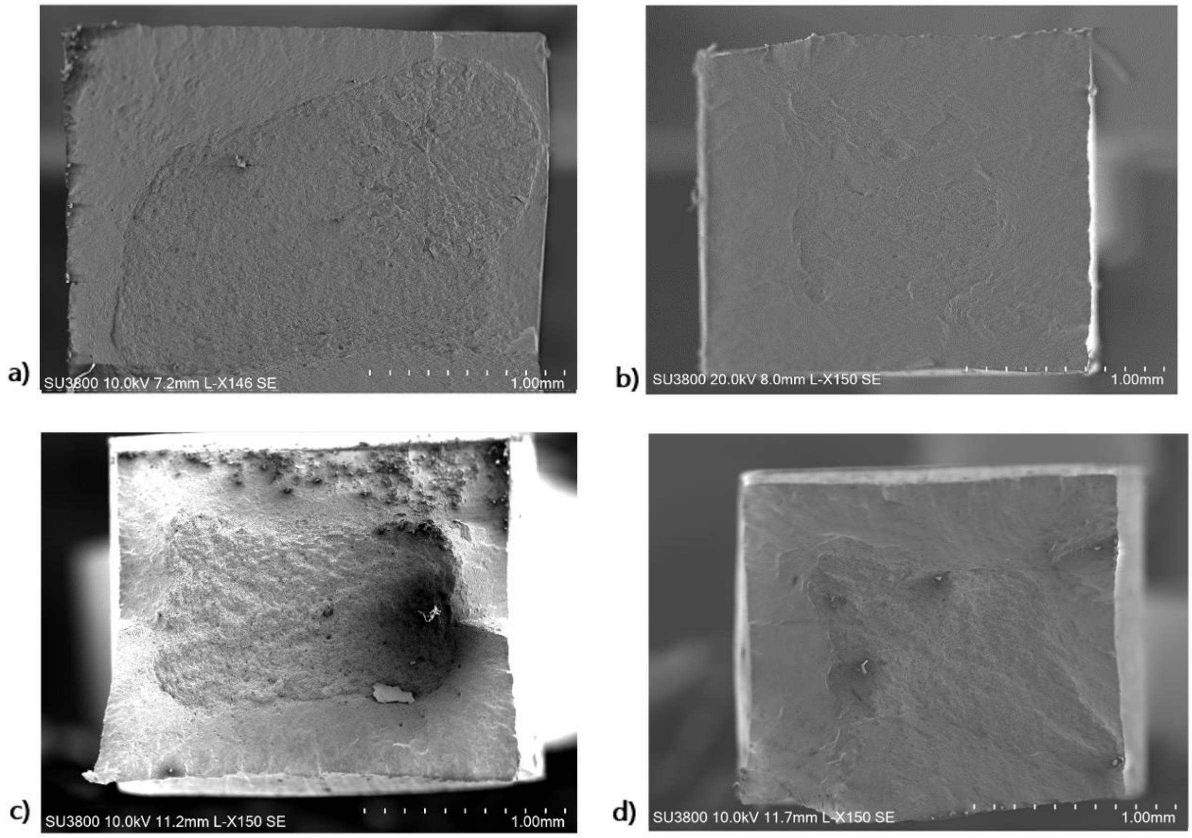

Figure 4.8 - Fracture surface of tensile samples at low magnification: a) Sample 13, b) Sample 7, c) Sample 8, d) Sample 5

Fracture surfaces of both heat-treated and as-deposited specimens exhibit a moderately ductile fracture. SEM fractography at low magnification revealed a rough and fully dimpled central region, indicating void nucleation and growth, with small and relatively flat shear lips in the outer region with only smaller voids, indicating limited but existing plastic deformation before failure. In short, the fracture surface is characterized by micro void coalescence dimples with shallow shear lips. As presented in the literature, fracture mechanics normally begin with the nucleation of voids at stress concentrators like inclusions or precipitates. As the tensile load increases, these voids are reported to grow and progressively link with neighboring voids, leading to the formation of internal cracks that contribute to the development of shear bands, particularly at the edges. In the central region, the growth and coalescence of voids are said to result in the characteristic dimpled morphology. Final fracture is understood to occur when the coalescing voids and shear bands merge into a continuous crack [52], [53].

To quantify the fracture surface morphology, the software "*ImageJ*" was used to determine the size of the dimples observed in the SEM images at Figure 4.9. A set of ten randomly chosen dimples was analyzed by measuring their width, providing a representative distribution of the fracture features. From this analysis, it was determined that the mean dimple width for Sample 5 was 6.079 $\pm$ 0.736 μm, while for Sample 7 the average width was slightly smaller, at 4,210 $\pm$ 0,601 μm.

In Figure 4.9b), the fracture surface of the as built maraging steel, sample 7, is shown in greater detail. The surface is dominated by a dimpled morphology with irregular size and distribution, characteristic of micro void nucleation and coalescence. The dimples are relatively shallow and non-uniform, suggesting that voids initiated at inclusions or fine precipitates within the martensitic matrix. Their limited growth is attributed to the high density of nucleated dimples, which generate a state of near-isostatic stress that restricts further cavity expansion. This is an indication of a ductile fracture mechanism, though not a fully developed ductile response, which is consistent with the moderate plasticity typically reported for as-built DED-Arc maraging steels [26], [53], [54].

Upon aging, Figure 4.9.a), presents a ductile fracture surface characterized primarily by micro-void coalescence, yet with noticeable heterogeneity in dimple size and shape. The dimples are generally larger and deeper than those observed in the as-built condition, see Figure 4.9.b), which is consistent with the precipitation of intermetallic compounds during aging, that serve as void nucleation sites [23], [49]. This morphological inconsistency can be attributed to the absence of a preceding solution annealing treatment, which plays a critical role in dissolving segregation and homogenizing the matrix before aging. Without this step, residual dendritic structures and segregation zones from the as-deposited condition may remain, resulting in a non-uniform distribution of strengthening precipitates during aging, consequently irregular features are formed, indicating localized variations in mechanical properties [26], [27].

Despite the microstructural inconsistencies, the fractured surface of the aged sample clearly exhibits a ductile failure mode, with no evidence of cleavage planes, intergranular cracking, river patterns, or quasi-cleavage facets, all of which are indicators of embrittlement or severe over-aging. However, the dimples are large and heterogeneous, suggesting that while precipitation hardening occurred, the absence of a prior solution annealing treatment limited microstructural homogenization and the presence of larger dimples reflects a condition close to overaging [27], [52], [54].

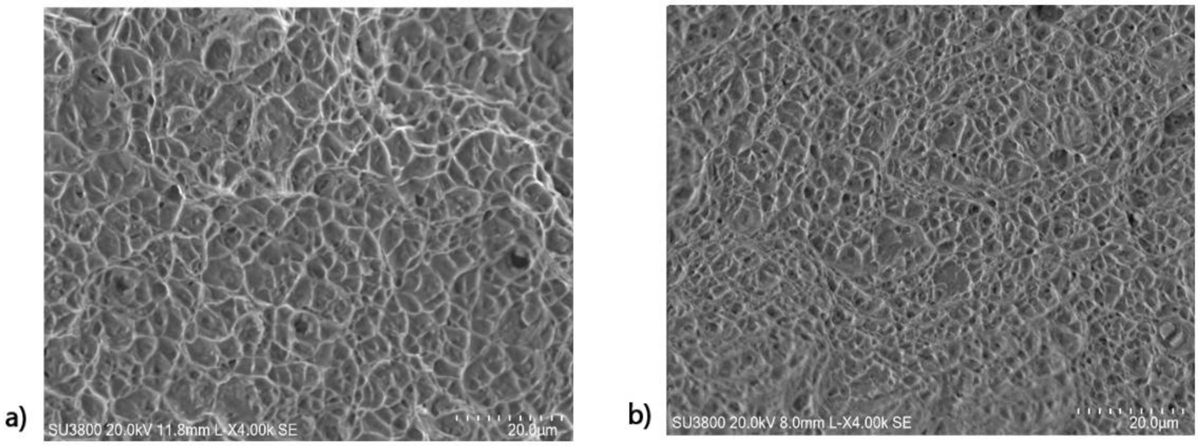

Figure 4.9 - Fracture surface of horizontal tensile samples at high magnification: a) Sample 5 (heat treated), b) Sample 7 (as built)

Comparing horizontal (Sample 5) and vertical (Sample 8) DED-Arc maraging steel samples (see Figure 4.8), notable differences in fracture surface morphology were observed, directly linked to the build orientation and microstructural anisotropy. For the vertical sample (Sample 8), with tensile load is applied perpendicular to the deposited layers, cracks propagate between the layers, following the weaker interlayer boundaries. This results in a rougher, more tortuous fracture surface, exacerbated by the alignment of columnar grains and residual stress anisotropy, which collectively promote void nucleation and irregular crack paths. In contrast, the horizontal sample (Sample 5), with the tensile load applied parallel to the deposited layers, exhibits cracks propagating predominantly along the layers, producing a relatively flatter fracture surface. Because the crack path in this orientation does not cross multiple layer interfaces, the influence of process-induced anisotropy on fracture behavior is significantly reduced [26], [27], [52].

5 Conclusions and Future Work

5.1 Conclusions

This work had as its primary purpose the optimization of DED-Arc for a Maraging steel UTP A 702 and the assessment of post-process heat treatment. Based on the experiments and characterization carried out in this thesis, it is possible to conclude the following:

- The short-circuit period was found to behave in strongly stochastic way, resulting in statistically significant effects but poor predictive fit. The voltage amplitude method is a more reliable choice for DoE.
- Arc Stability was found to be the most dependent on wire feed speed (WFS) and voltage, whereas travel speed was not significant.
- Response surface plots reveal the interplay between heat input and deposition rate, indicating the need for multivariable optimization, with the regression model predicting the optimal parameters of TS = 481.4 mm/min, WFS = 5.9 mm/min, V = 23.4 V, that maximize the arc stability index at 96.3%.
- In the as-built condition, vertical samples showed higher strength and ductility (UTS = 1366 MPa, Elongation = 6.7%) than horizontal samples (UTS = 1253 MPa, elongation = 5.9%).
- Direct aging heat treatment improved strength and ductility, for vertical samples UTS = 1613.3 MPa, Elongation = 8.5% and for horizontal UTS = 1686.7 MPa, Elongation = 10.17%.
- For the deposited wall, the microstructure varied along the build height. The base contained coarse columnar martensite with retained austenite, the middle showed finer martensite laths and some austenite and the top exhibit fine dendritic martensite with little austenite.
- Some over-aging was observed, as it led to the increase in size of martensite grains and quantity of reverted austenite.

- After aging, there was an increase in reverted austenite especially at bottom and middle regions, coarsened martensite laths and wider grain boundaries. The overall matrix remained martensitic with dispersed precipitates and reverted austenite in grain boundaries and inter dendritic areas.
- Fractography indicated predominantly ductile failure across all conditions, confirmed by a dimpled morphology and void nucleation at precipitates or inclusions. The increase in dimple size compared to the as built samples is consistent with the strengthening and growth of precipitates that serve as void nucleation sites.
- The lack of solution annealing before aging contributed to the heterogeneity in the microstructure. Without this step there was an uneven distribution of precipitates during aging, explaining the irregular dimple sizes.

5.2 Future Work

Some improvements and proposals for future work are suggested in this section.

Most of the articles used as references in the development of this work address additive manufacturing of maraging steels with a focus on DED-Arc using GTAW and DED-Arc using CMT technology, so it is proposed to study these processes for maraging steels, for example using CMT to investigate the manufacturing of large-scale components, Cold Metal Transfer typically provides much lower and better-controlled heat input, reduced distortion, low spatter, improved deposition efficiency and easier dimensional control which benefits productivity and reduces post-processing. Expected CMT-deposited UTP A 702 should show reduced anisotropy, lower fraction of retained/reverted austenite throughout the build and aged samples, lower scatter between specimens, and reduced residual-stress–driven distortion. The DED-Arc with GTAW could be used for smaller, higher-quality parts for aerospace or military sectors.

The use of Design of Experiments (DoE) can be further studied, there is a lack of scientific publications that address this topic. It was concluded that the deposition of maraging steels evolves a larger factor of welding parameters, so it's proposed a two-step approach for the DoE of this process. An initial screening stage using fractional factorial to screen the most influential welding parameters and a second approach using the same methodology was demonstrated in this study.

Additionally, it´s recommended to improve the experimental setup by employing higher performance equipment and study the impact of different heat treatments, such as solution annealing and aging treatment at different temperatures and holding times and the method of cooling, like air cooling or furnace cooling.

BIBLIOGRAPHY

[1] T. A. Rodrigues, V. Duarte, J. A. Avila, T. G. Santos, R. M. Miranda, and J. P. Oliveira, "Wire and arc additive manufacturing of HSLA steel: Effect of thermal cycles on microstructure and mechanical properties," *Addit Manuf*, vol. 27, pp. 440–450, May 2019, doi: 10.1016/j.addma.2019.03.029.

[2] Y. peng LI *et al.*, "Research status and quality improvement of wire arc additive manufacturing of metals," *Transactions of Nonferrous Metals Society of China (English Edition)*, vol. 33, no. 4, pp. 969–996, Apr. 2023, doi: 10.1016/S1003-6326(23)66160-6.

[3] Y. Li, C. Su, and J. Zhu, "Comprehensive review of wire arc additive manufacturing: Hardware system, physical process, monitoring, property characterization, application and future prospects," *Results in Engineering*, vol. 13, pp. 100–330, Mar. 2022, doi: 10.1016/j.rineng.2021.100330.

[4] V. R. Duarte, "Additive manufacturing of a high resistance steel by MIG/MAG," NOVA University Lisbon, 2016.

[5] T. A. Rodrigues, V. Duarte, R. M. Miranda, T. G. Santos, and J. P. Oliveira, "Current status and perspectives on wire and arc additive manufacturing (WAAM)," *Materials*, vol. 12, no. 12, Apr. 2019, doi: 10.3390/ma12071121.

[6] ISO/ASTM International, "Additive manufacturing — General principles — Fundamentals and vocabulary," ISO/ASTM 52900:2021, 2021

[7] K. V. Wong and A. Hernandez, "A Review of Additive Manufacturing," *ISRN Mechanical Engineering*, vol. 2012, pp. 1–10, Aug. 2012, doi: 10.5402/2012/208760.

[8] V. R. Duarte, "DEVELOPMENTS IN DIRECTED ENERGY DEPOSITION ADDITIVE MANUFACTURING: IN-SITU HOT FORGING AND INDIRECT COOLING," NOVA University Lisbon, 2022.

[9] T. M. A. Rodrigues, "Improvement and tailoring of parts fabricated with Wire and Arc Additive Manufacturing," NOVA University Lisbon, 2022. [Online]. Available: https://run.unl.pt/handle/10362/150178

[10] K. S. B. Ribeiro, F. E. Mariani, and R. T. Coelho, "A Study of Different Deposition Strategies in Direct Energy Deposition (DED) Processes," *Procedia Manuf*, vol. 48, pp. 663–670, 2020, doi: 10.1016/j.promfg.2020.05.158.

[11] K. Li *et al.*, "A critical review on wire-arc directed energy deposition of high-performance steels," May 01, 2023, *Elsevier Editora Ltda*. doi: 10.1016/j.jmrt.2023.05.163.

[12] M. S. Mohd Mansor *et al.*, "Integrated approach to Wire Arc Additive Manufacturing (WAAM) optimization: Harnessing the synergy of process parameters and deposition strategies," *Journal of Materials Research and Technology*, vol. 30, pp. 2478–2499, May 2024, doi: 10.1016/j.jmrt.2024.03.170.

[13] B. Tomar, S. Shiva, and T. Nath, "A review on wire arc additive manufacturing: Processing parameters, defects, quality improvement and recent advances," Jun. 01, 2022, *Elsevier Ltd*. doi: 10.1016/j.mtcomm.2022.103739.

[14] H. Iqbal, A. Ascari, E. Liverani, and A. Fortunato, "Analysis of process parameters, deposition strategies and build orientations in wire-arc additive manufacturing (WAAM)," *Progress in Additive Manufacturing*, 2024, doi: 10.1007/s40964-024-00938-w.

[15] T. M. A. Rodrigues, "Wire and arc additive manufacturing : equipment development and parts characterization," NOVA University Lisbon, 2018.

[16] E. Puñales and S. Alfaro, "Stability on the GMAW Process," *IntechOpen*, 2020, [Online]. Available: www.intechopen.com

[17] A. C. S. Faria, "Study of a hardfacing flux-cored wire for Wire and Arc Additive Manufacturing applications," Instituto Superior Técnico, 2019.

[18] M. Rashid, S. Sabu, A. Kunjachan, M. Agilan, T. Anjilivelil, and J. Joseph, "'Advances in wire-arc additive manufacturing of nickel-based superalloys: Heat sources, DfAM principles, material evaluation, process parameters, defect management, corrosion evaluation and post-processing techniques,'" Nov. 01, 2024, *KeAi Publishing Communications Ltd*. doi: 10.1016/j.ijlmm.2024.05.009.

[19] W. Hackenhaar, J. A. E. Mazzaferro, C. C. P. Mazzaferro, N. Grossi, and G. Campatelli, "Effects of different WAAM current deposition modes on the mechanical properties of AISI H13 tool steel," *Welding in the World*, vol. 66, no. 11, pp. 2259–2269, Nov. 2022, doi: 10.1007/s40194-022-01342-0.

[20] T. Chen, S. Xue, B. Wang, P. Zhai, and W. Long, "Study on short-circuiting GMAW pool behavior and microstructure of the weld with different waveform control methods," *Metals (Basel)*, vol. 9, no. 12, Dec. 2019, doi: 10.3390/met9121326.

[21] F. Veiga, A. Suárez, E. Aldalur, and T. Bhujangrao, "Effect of the metal transfer mode on the symmetry of bead geometry in waam aluminum," *Symmetry (Basel)*, vol. 13, no. 7, Jul. 2021, doi: 10.3390/sym13071245.

[22] J. Zhang, J. Fan, L. Duan, W. Chen, D. Yang, and K. Wang, “Effect of heat treatment on the microstructure and mechanical properties of 18Ni 300 maraging steel manufactured by wire + arc additive manufacturing,” *Virtual Phys Prototyp*, vol. 19, no. 1, 2024, doi: 10.1080/17452759.2024.2397007.

[23] R. Ge *et al.*, “Effect of heat treatment on microstructure and mechanical properties of 18Ni-350 maraging steel fabricated by Wire and Arc Additive Manufacturing,” *Mater Today Commun*, vol. 40, Aug. 2024, doi: 10.1016/j.mtcomm.2024.109793.

[24] L. Kučerová, K. Burdová, Š. Jeníček, and J. Volkmannová, “Microstructure and Mechanical Properties of 3D Printed Tool Steel after Various Precipitation Hardening Treatments,” *Manufacturing Technology*, vol. 22, no. 2, pp. 185–191, 2022, doi: 10.21062/mft.2022.030.

[25] L. Guo, L. Zhang, J. Andersson, and O. Ojo, “Solidification structures and phases in wire arc additive manufactured C250 maraging steel,” *Materials Science and Technology (United Kingdom)*, vol. 39, no. 5, pp. 582–590, 2023, doi: 10.1080/02670836.2022.2128577.

[26] X. Xu, S. Ganguly, J. Ding, S. Guo, S. Williams, and F. Martina, “Microstructural evolution and mechanical properties of maraging steel produced by wire + arc additive manufacture process,” *Mater Charact*, vol. 143, pp. 152–162, Sep. 2018, doi: 10.1016/j.matchar.2017.12.002.

[27] W. Xiaowei, Y. Dongqing, H. Yong, Z. Qi, F. Jikang, and W. Kehong, “Microstructure and Mechanical Properties of As-Deposited and Heat-Treated 18Ni (350) Maraging Steel Fabricated by Gas Metal Arc-Based Wire and Arc Additive Manufacturing,” *J Mater Eng Perform*, vol. 30, no. 9, pp. 6972–6981, Sep. 2021, doi: 10.1007/s11665-021-06102-7.

[28] A. M. F. Rocha, “Fabrico Aditivo de Fio por Arco elétrico com Forjamento a quente in-situ de Ti-6Al-4V e Cobre,” NOVA University Lisbon, 2023.

[29] D. A. E. Amendoeira, “EVALUATION OF THE INFLUENCE OF NOZZLE COOLING DURING THE HOT FORGING WIRE AND ARC ADDITIVE,” NOVA University Lisbon, 2023.

[30] N. Kumar *et al.*, “Wire Arc Additive Manufacturing – A revolutionary method in additive manufacturing,” *Mater Chem Phys*, vol. 285, Jun. 2022, doi: 10.1016/j.matchemphys.2022.126144.

[31] F. R. P. dos Santos, “Hot-Forging WAAM de aço de baixa liga,” NOVA University Lisbon, 2021.

[32] V. R. Duarte, T. A. Rodrigues, N. Schell, R. M. Miranda, J. P. Oliveira, and T. G. Santos, "In-situ hot forging directed energy deposition-arc of CuAl8 alloy," *Addit Manuf*, vol. 55, Jul. 2022, doi: 10.1016/j.addma.2022.102847.

[33] C. Kan, L. Zhao, Y. Cao, C. Ma, Y. Peng, and Z. Tian, "Microstructure evolution and strengthening behavior of maraging steel fabricated by wire arc additive manufacturing at different heat treatment processes," *Materials Science and Engineering: A*, vol. 909, Sep. 2024, doi: 10.1016/j.msea.2024.146804.

[34] F. F. Conde, J. D. Escobar, J. P. Oliveira, A. L. Jardini, W. W. Bose Filho, and J. A. Avila, "Austenite reversion kinetics and stability during tempering of an additively manufactured maraging 300 steel," *Addit Manuf*, vol. 29, Oct. 2019, doi: 10.1016/j.addma.2019.100804.

[35] Voestalpine, "UTP A 702," Mar. 2014.

[36] Voestalpine BÖHLER Edelstahl GmbH & Co KG, "BÖHLER W722 VMR – Hot Work Tool Steels," Kapfenberg, Áustria, 2024. [Online]. Available: https://www.voestalpine.com/bohler-edelstahl/de/

[37] D. P. M. da Fonseca, A. L. Melo Feitosa, L. G. de Carvalho, R. L. Plaut, and A. F. Padilha, "A short review on ultra-high-strength maraging steels and future perspectives," 2021, *Universidade Federal de Sao Carlos*. doi: 10.1590/1980-5373-MR-2020-0470.

[38] J. Viňáš, J. Brezinová, M. Pástor, P. Šarga, M. Džupon, and J. Brezina, "Determination of the Effect of Heat Input during Laser Welding on the Magnitude of Residual Stresses in the Refurbishment of Al Alloy Casting," *Metals (Basel)*, vol. 13, no. 12, Dec. 2023, doi: 10.3390/met13122003.

[39] F. Pixner *et al.*, "Influence of process and heat input on the microstructure and mechanical properties in wire arc additive manufacturing of hot work tool steels," *Materials Science and Engineering: A*, vol. 888, Nov. 2023, doi: 10.1016/j.msea.2023.145799.

[40] H. Berns, V. Gavriljuk, and B. Shanina, "Intensive interstitial strengthening of stainless steels," *Adv Eng Mater*, vol. 10, no. 12, pp. 1083–1093, Dec. 2008, doi: 10.1002/adem.200800214.

[41] R. Madesh and G. K. K., "Multi-layer additive manufacturing on nickel-based superalloy by optimization of pulsed mode process parameters of single-layer bead geometry," *Mater Today Commun*, vol. 37, Dec. 2023, doi: 10.1016/j.mtcomm.2023.107463.

[42] C. Machado, "Modelos Estatísticos para a Caracterização de Texturas Produzidas por Electroerosão," Faculdade de Ciências e Tecnologia , Lisbon, 2002.

[43] D. C. . Montgomery, *Design and analysis of experiments*, 8th ed. Hoboken, NJ: John Wiley & Sons, Inc., 2013.

[44] J. McNicol, B. Narayanan, N. Sridhar, and C. Fink, "Corrosion resistance of austenitic stainless steel welds with no-backing gas," *Welding in the World*, vol. 67, no. 3, pp. 819–830, Mar. 2023, doi: 10.1007/s40194-022-01442-x.

[45] M. Suban and J. Tušek, "Methods for the determination of arc stability," in *Journal of Materials Processing Technology*, Dec. 2003, pp. 430–437. doi: 10.1016/S0924-0136(03)00416-3.

[46] TEP Engineering S.r.l., *STEP Lab Mechanical Testing Machines Catalog*. 2023. [Online]. Available: www.step-lab.com

[47] The British Standards Institution 2020, "Metallic materials - Tensile testing Part 1, Method of test at room temperature," 2020

[48] Y. R. Wong and S. F. Ling, "An investigation of dynamical metal transfer in GMAW - Effects of argon shielding gas," *J Mater Process Technol*, vol. 214, no. 1, pp. 106–111, 2014, doi: 10.1016/j.jmatprotec.2013.08.003.

[49] M. Niu, G. Zhou, W. Wang, M. B. Shahzad, Y. Shan, and K. Yang, "Precipitate evolution and strengthening behavior during aging process in a 2.5 GPa grade maraging steel," *Acta Mater*, vol. 179, pp. 296–307, Oct. 2019, doi: 10.1016/j.actamat.2019.08.042.

[50] W. Callister and D. Rethwisch, *Materials Science and Engineering An Introduction*, Tenth edition. Wiley.

[51] F. Tariq, M. Shifa, and R. A. Baloch, "Effect of Overaging Conditions on Microstructure and Mechanical Properties of Maraging Steel," *Metal Science and Heat Treatment*, vol. 62, no. 3–4, pp. 188–194, Jul. 2020, doi: 10.1007/s11041-020-00535-y.

[52] R. Hertzberg, *Deformation and Fracture Mechanics of Engineering Materials*, Fourth Edition. John Wiley & Sons, INC., 1996.

[53] T. L. Anderson, *FRACTURE MECHANICS - Fundamentals and Aplications*, Fourth Edition. CRC Press, 2017.

[54] H. J. Rack and D. Kalish, "The Strength and Fracture Toughness of 18 Ni (350) Maraging Steel," *Metallurgical Transactions*, vol. Volume 2, Oct. 1971.

APPENDIX

Appendix A

Code used on the arc stability using the short-circuit period method.

```
import os
import numpy as np
import matplotlib.pyplot as plt
from scipy.signal import iirnotch, filtfilt

# Configuration

FILE_PATH       = r'C:\Users\Asus\Desktop\Tese\Dados_LAb\Exper_4\UTPA_702_n47.txt'
FS              = 10000     # Sampling rate [Hz]
VOLTAGE_SCALE     = 30.8745
CURRENT_SCALE     = 149.4586

V_THRESHOLD       = 9        # Voltage dip detect threshold [V]
MIN_SEPARATION_MS = 25       # Minimum ms between dips [ms]
ARC_START_THRESHOLD = 10.0   # V threshold for arc start detection

T_START   = 2.5    # start counting dips 4.5 s after arc-start
N_CYCLES  = 30     # number of dips to use for ASI (pick 20..50)
NOTCH_FREQ = 50.0
Q_FACTOR   = 30.0


def notch_filter(signal, fs=FS, notch_freq=NOTCH_FREQ, q=Q_FACTOR):
    """
    Apply a 50 Hz notch filter to 'signal' (1D numpy array).
    """
    nyquist = 0.5 * fs
```

```
    w0 = notch_freq / nyquist
    b, a = iirnotch(w0, q)
    return filtfilt(b, a, signal)

def load_signal_data(filepath):
    """
    Load a whitespace-delimited text file that has (time, voltage_raw, current_raw),
    ignoring lines that start with '#' and stopping at a header line beginning with 'Time'.
    Returns three numpy arrays: time (s), voltage (scaled), current (scaled).
    """
    if not os.path.isfile(filepath):
        raise FileNotFoundError(f"Data file not found: {filepath}")

    time_list = []
    voltage_list = []
    current_list = []
    with open(filepath, 'r') as f:
        # Skip comments until we see a line starting with 'Time' (case-insensitive).
        for line in f:
            if line.lstrip().startswith('#'):
                continue
            if line.strip().lower().startswith('time'):
                # Found the header; now break to start reading numeric data
                break

        # Now read the actual numeric data lines:
        for line in f:
            cols = line.strip().split()
            if len(cols) >= 3:
                # First column = time (s), second = raw voltage, third = raw current
                time_list.append(float(cols[0]))
                voltage_list.append(float(cols[1]) * VOLTAGE_SCALE)
                current_list.append(float(cols[2]) * CURRENT_SCALE)
```

```
    return (
        np.array(time_list),
        np.array(voltage_list),
        np.array(current_list)
    )

def detect_voltage_dips(voltage, v_threshold=V_THRESHOLD, min_separation_ms=MIN_SEPARATION_MS):
    """
    Return the indices (into 'voltage') where voltage < v_threshold,
    but enforce at least min_separation_ms between consecutive indices.
    """
    dip_idxs = np.where(voltage < v_threshold)[0]
    if dip_idxs.size == 0:
        return np.array([], dtype=int)

    min_sep_samples = int((min_separation_ms / 1000.0) * FS)
    selected = [dip_idxs[0]]
    for idx in dip_idxs[1:]:
        if idx - selected[-1] > min_sep_samples:
            selected.append(idx)
    return np.array(selected, dtype=int)

def plot_signal(time, signal, title, ylabel, color='tab:blue'):
    """
    Plot 'signal' vs. 'time' (both 1D arrays), draw a vertical line at t=0,
    and label axes.
    """
    plt.figure(figsize=(10, 4))
    plt.plot(time, signal, color=color, linewidth=1)
    plt.axvline(0.0, color='gray', linestyle='--', label='Arc Start (t=0)')
    plt.title(title)
    plt.xlabel("Time since weld start (s)")
    plt.ylabel(ylabel)
```

```
    plt.legend()
    plt.grid(True)
    plt.tight_layout()
    plt.show()

def plot_events(time, signal, event_idxs, title):
    """
    Plot 'signal' vs. 'time', and mark points at indices 'event_idxs' with red 'x'.
    """
    plt.figure(figsize=(10, 4))
    plt.plot(time, signal, label="Voltage (Filtered)", color='tab:blue')
    if event_idxs.size > 0:
        plt.plot(time[event_idxs], signal[event_idxs], 'rx', label='Detected Dips')
    plt.title(title)
    plt.xlabel("Time since weld start (s)")
    plt.ylabel("Voltage (V)")
    plt.legend()
    plt.grid(True)
    plt.tight_layout()
    plt.show()

# Main processing

def main():
    # 1) Load raw data
    time_raw, voltage_raw, current_raw = load_signal_data(FILE_PATH)

    # 2) Find arc-start index (first sample above ARC_START_THRESHOLD)
    arc_idxs = np.where(voltage_raw > ARC_START_THRESHOLD)[0]
    if arc_idxs.size == 0:
        raise RuntimeError(
            "No arc-start detected. "
            "Either the file has no samples above ARC_START_THRESHOLD, "
            "or ARC_START_THRESHOLD is too high."
```

```
    )
    i0 = arc_idxs[0]
    t0 = time_raw[i0]
    print(f"Arc start detected at index {i0}, t0 = {t0:.6f} s (V={voltage_raw[i0]:.2f} V)")

    # 3) Shift time so that t0 → 0
    time = time_raw - t0
    voltage = voltage_raw.copy()
    current = current_raw.copy()

    # 4) Notch-filter both channels
    voltage_filt = notch_filter(voltage)
    current_filt = notch_filter(current)

    # 5) Detect ALL dips (below V_THRESHOLD) in the filtered voltage
    all_dip_idxs = detect_voltage_dips(voltage_filt)
    all_dip_times = time[all_dip_idxs]

    # 6) Keep only dips after T_START
    mask_after_start = (all_dip_times >= T_START)
    dips_after_start = all_dip_times[mask_after_start]

    # 7) Ensure we have at least N_CYCLES dips
    if dips_after_start.size < N_CYCLES:
        raise RuntimeError(
            f"Only {dips_after_start.size} dips found after {T_START:.2f} s; "
            f"cannot compute ASI with N_CYCLES={N_CYCLES}"
        )

    # 8) Truncate to exactly N_CYCLES dips
    dips_to_use = dips_after_start[:N_CYCLES]

    # 9) Compute the intervals (in seconds) between those N_CYCLES dips ( => N_CY-
CLES - 1 intervals )
```

```
intervals = np.diff(dips_to_use)
mean_T = np.mean(intervals)
std_T = np.std(intervals, ddof=1)
asi = 100.0 * (1.0 - std_T / mean_T) if mean_T != 0 else 0.0

# 10) Print ASI results
print("\n--- Arc Stability Index (ASI) ---")
print(f"  Using first {N_CYCLES} dips after {T_START:.2f} s:")
print(f"    Mean Period     : {mean_T * 1000.0:.2f} ms")
print(f"    Std Dev Period  : {std_T * 1000.0:.2f} ms")
print(f"    ASI             : {asi:.2f} %")

# 11) Save the N_CYCLES dip-times to a text file
np.savetxt(
    "detected_events.txt",
    dips_to_use,
    fmt="%.6f",
    header="Event times (s since arc-start)"
)

# 12) Plot 1: Full filtered voltage vs. time, marking all dip locations
plot_signal(time, voltage_filt, "Full Voltage (50 Hz Notch)", "Voltage (V)")

#    We'll also mark *all* dips for visualization:
if all_dip_idxs.size > 0:
    plot_events(time, voltage_filt, all_dip_idxs, "All Detected Dips (Filtered Voltage)")

# 13) Plot 2: Zoom-in on [T_START .. (time of Nth dip + 10 ms)], marking exactly the
chosen N_CYCLES dips

t_plot_start = T_START
t_plot_end = dips_to_use[-1] + 0.010  # 10 ms margin past the last chosen dip

# Mask for that window:
```

```
        mask_plot = (time >= t_plot_start) & (time <= t_plot_end)
        time_win = time[mask_plot]
        volt_filt_win = voltage_filt[mask_plot]

        # Find the indices *within* 'time_win' that correspond to 'dips_to_use'.
        # We'll simply take each dip time, find the nearest sample index in the full 'time'
array,
        # then check if it lies inside [t_plot_start, t_plot_end], and convert to the local
'time_win' index.
        chosen_dip_idxs_in_win = []
        for dip_t in dips_to_use:
            # find the global index in 'time' closest to dip_t:
            global_idx = np.argmin(np.abs(time - dip_t))
            if t_plot_start <= time[global_idx] <= t_plot_end:
                # now find where that sits in the sliced window:
                local_idx = np.where(mask_plot)[0].tolist().index(global_idx)
                chosen_dip_idxs_in_win.append(local_idx)

        chosen_dip_idxs_in_win = np.array(chosen_dip_idxs_in_win, dtype=int)

        plot_events(
            time_win,
            volt_filt_win,
            chosen_dip_idxs_in_win,
            f"Voltage Dips Used for S (First {N_CYCLES} Dips After {T_START:.2f} s)"
        )

if __name__ == "__main__":
    main()
```

Appendix B

Code used on the arc stability using the short-circuit voltage method

```
import numpy as np
import matplotlib.pyplot as plt
```

```
from scipy.signal import butter, filtfilt
import seaborn as sns  # for histogram visualization

# --------------------------
# Configuration
# --------------------------
FILE_PATH = r'C:\Users\Asus\Desktop\Tese\Dados_Lab\Exper_1\UTPA_702_n40.txt'
FS = 10000                      # Sampling frequency (Hz)
T_START = 5                     # Start time for slicing (s)
T_END = 10                      # End time for slicing (s)
VOLTAGE_SCALE = 30.8745         # Scale factor for voltage
CUTOFF_FREQ = 500               # Low-pass filter cutoff (Hz)
FILTER_ORDER = 4                # Filter order

# --------------------------
# Low-pass filter
# --------------------------
def lowpass_filter(data, fs, cutoff, order):
    nyq = 0.5 * fs
    normal_cutoff = cutoff / nyq
    b, a = butter(order, normal_cutoff, btype='low', analog=False)
    return filtfilt(b, a, data)

# --------------------------
# Data Loading
# --------------------------
def load_signal_data(filepath):
    time, voltage = [], []
    with open(filepath, 'r') as f:
        for line in f:
            if line.lstrip().startswith('#'):
                continue
            if line.strip().startswith('Time'):
                break
```

```
        for line in f:
            cols = line.strip().split()
            if len(cols) >= 2:
                time.append(float(cols[0]))
                voltage.append(float(cols[1]) * VOLTAGE_SCALE)
    return np.array(time), np.array(voltage)

# --------------------------
# Time-based Slicing
# --------------------------
def slice_interval(time, voltage, t_start, t_end):
    mask = (time >= t_start) & (time <= t_end)
    return time[mask], voltage[mask]

# --------------------------
# Voltage-based Stability
# --------------------------
def compute_voltage_based_stability(voltage):
    mu_v = np.mean(voltage)
    sigma_v = np.std(voltage)
    if mu_v != 0:
        return 100.0 * (1 - sigma_v / mu_v), mu_v
    return None, mu_v

# --------------------------
# Plots
# --------------------------
def plot_voltage_signal(time, voltage):
    plt.figure(figsize=(10, 4))
    plt.plot(time, voltage, label="Voltage")
    plt.axvline(T_START, color='green', linestyle='--', label='Start')
    plt.axvline(T_END, color='red', linestyle='--', label='End')
    plt.title("Voltage Signal")
    plt.xlabel("Time (s)")
```

```
    plt.ylabel("Voltage (V)")
    plt.legend()
    plt.grid()
    plt.tight_layout()
    plt.show()

def plot_voltage_histogram(voltage):
    plt.figure(figsize=(6, 4))
    sns.histplot(voltage, bins=50, kde=True)
    plt.title("Voltage Distribution")
    plt.xlabel("Voltage (V)")
    plt.ylabel("Frequency")
    plt.tight_layout()
    plt.show()

# --------------------------
# Main
# --------------------------
def main():
    # Load and filter
    time, voltage = load_signal_data(FILE_PATH)
    voltage = lowpass_filter(voltage, FS, CUTOFF_FREQ, FILTER_ORDER)

    # Plot raw & filtered window
    plot_voltage_signal(time, voltage)

    # Slice by time
    time_win, volt_win = slice_interval(time, voltage, T_START, T_END)

    # Histogram for distribution check
    plot_voltage_histogram(volt_win)

    # Compute ASI and mean voltage
    asi, mean_voltage = compute_voltage_based_stability(volt_win)
```

```
    if asi is not None:
        print(f"Arc Stability Index (Voltage-Based): {asi:.2f}%")
        print(f"Mean Voltage: {mean_voltage:.2f} V")
    else:
        print("Cannot compute ASI (mean voltage = 0)")


if __name__ == "__main__":
    main()
```

Appendix C

DoE Contour plots for voltage based arc stability

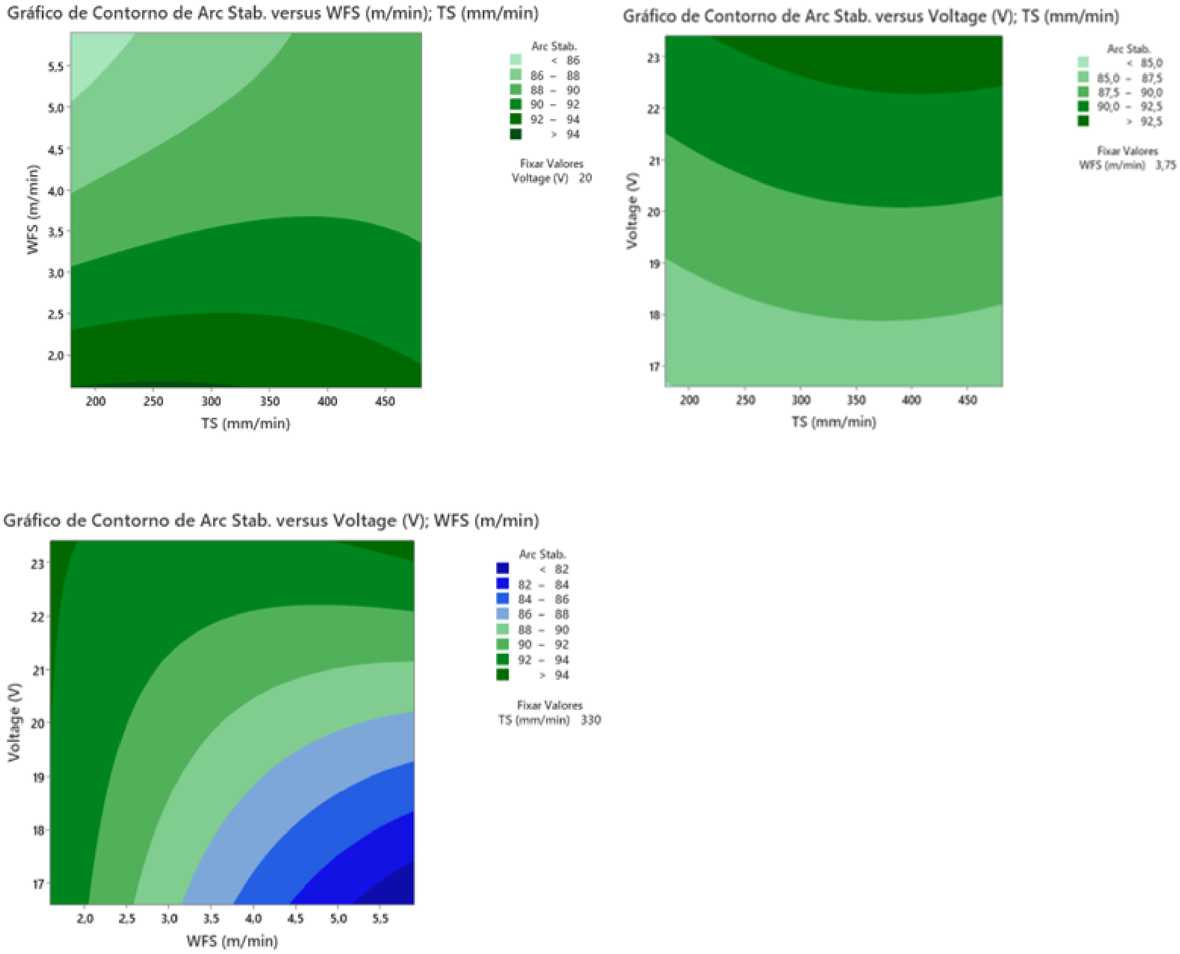

Appendix D

Uniaxial tensile samples after fracture

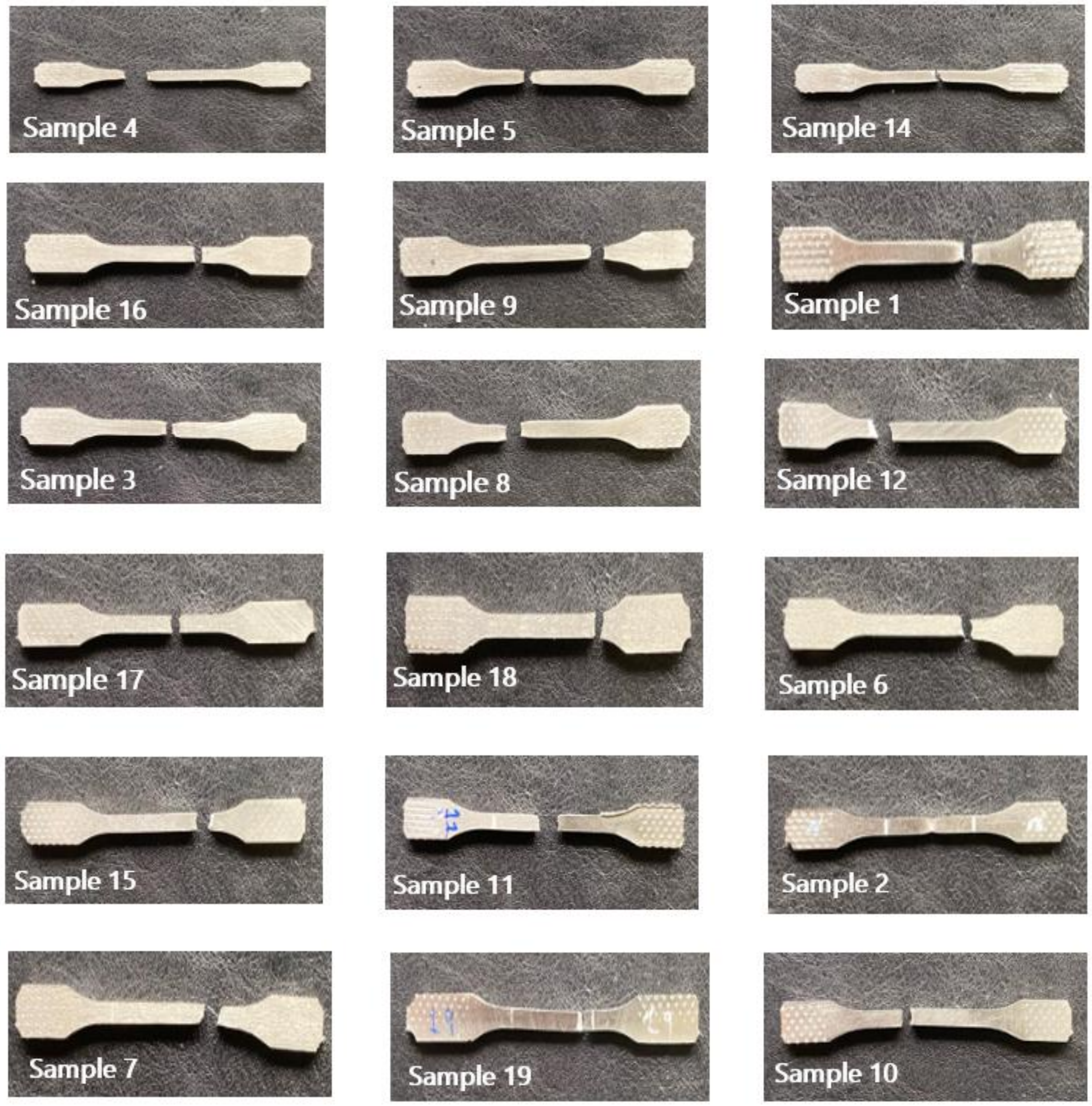

Appendix E

Results from the uniaxial tensile test

	Sample Number	Direction	UTS	YS	Elongation
Without Heat treatment	2	Vertical	1340	360	0.095
	6	Horizontal	1370	388	0.097
	7	Horizontal	1290	508	0.057
	10	Vertical	1230	392	0.058
	11	Vertical	1380	652	0.073
	12	Vertical	1330	460	0.061

	13	Vertical	1490	457	0.068
	15	Horizontal	1280	383	0.063
	17	Horizontal	845	360	0.04
	18	Horizontal	925	456	0.038
	19	Horizontal	1190	377	0.056
With Heat treatment	1	Vertical	1650	943	0.080
	3	Vertical	1650	874	0.084
	4	Horizontal	1450	710	0.083
	5	Horizontal	1700	901	0.12
	8	Vertical	1540	720	0.09
	9	Vertical	1620	844	0.093
	14	Horizontal	1650	696	0.12
	16	Horizontal	1710	750	0.065

Appendix F

Fracture surfaces analyzed on SEM

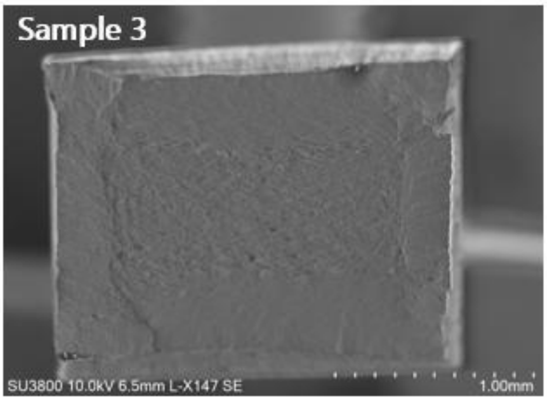

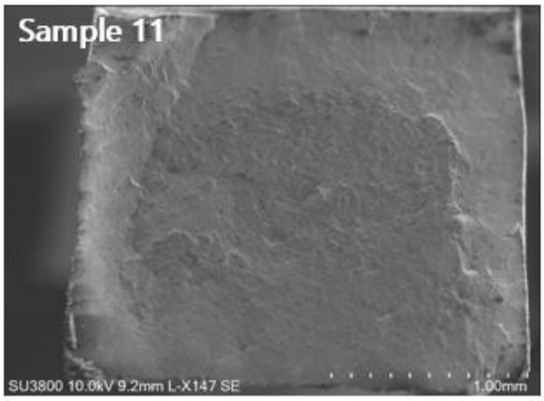

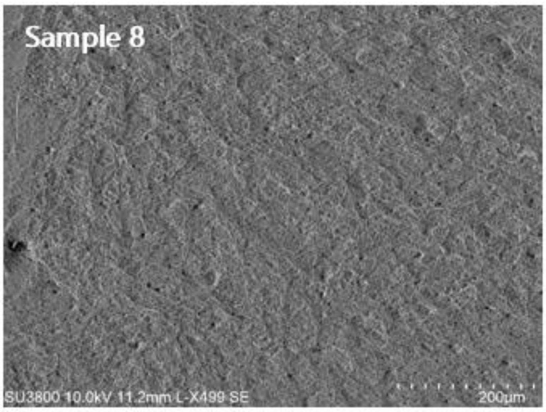
Sample 8
SU3800 10.0kV 11.2mm L-X499 SE
200μm

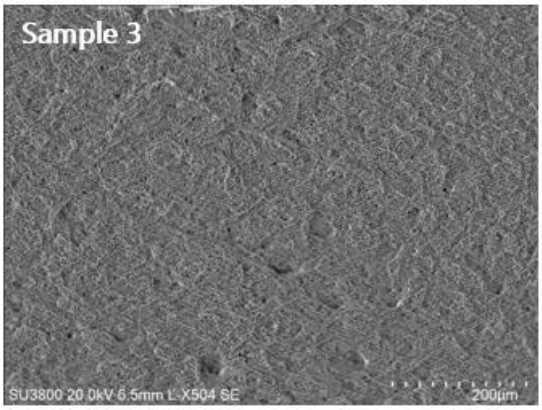
Sample 3
SU3800 20.0kV 6.5mm L-X504 SE
200μm

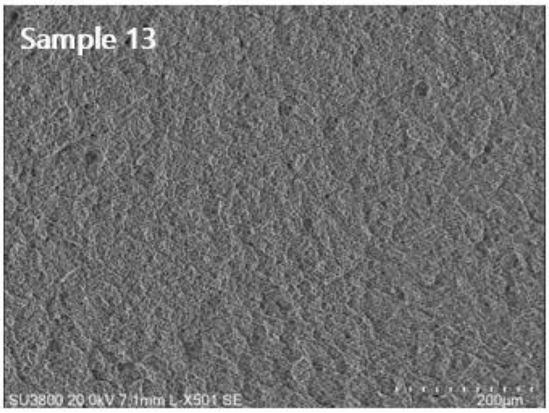
Sample 13
SU3800 20.0kV 7.1mm L-X501 SE
200μm

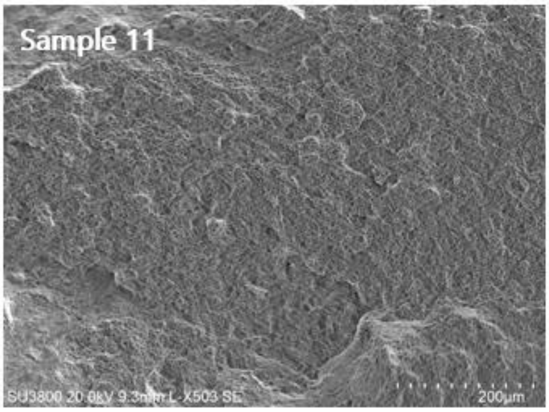
Sample 11
SU3800 20.0kV 9.3mm L-X503 SE
200μm

2025

Guilherme Gamito

Maraging Steel Fabricated via Directed Energy Deposition: Process Parameters Development and Study of the Post-Deposition Aging Heat Treatment

NOVA SCHOOL OF SCIENCE & TECHNOLOGY